https://doi.org/10.5194/egusphere-2025-1865
Preprint. Discussion started: 26 May 2025

Simulation of a contrail formation and early life cycle for a realistic airliner geometry

Younes Bouhafid[1] and Nicolas Bonne[2]

[1]ONERA, DAAA, Université Paris-Saclay F-91123, Palaiseau, France
[2]ONERA, DMPE, Université Paris-Saclay F-91123, Palaiseau, France

Correspondence: Younes Bouhafid (younes.bouhafid@onera.fr)

Abstract. Contrails—ice clouds that form in aircraft wakes—are thought to have a radiative impact up to twice that of CO2 emissions, although this estimate remains debated due to significant uncertainties. These uncertainties underline the need for further research into the entire life cycle of contrails, from the formation of initial ice crystals to their potential evolution into persistent cirrus clouds. The challenge lies in the wide range of spatial and temporal scales involved in contrail development.

This work presents a novel numerical methodology for simulating contrails from the onset of ice crystal formation to the dissipation of wingtip vortices. Unlike conventional methods that rely on analytical initialization, our approach couples Reynolds-averaged Navier–Stokes (RANS) with Large Eddy Simulation (LES) and synthetic turbulence techniques. This allows for a more accurate capture of near-field effects and a detailed consideration of how aircraft geometry influences the aerodynamic wake and subsequent contrail evolution.

Applied to a realistic aircraft under standard atmospheric conditions, our methodology revealed that horizontal tailplane vortices can trigger short-wavelength instabilities in wingtip vortices, significantly modifying the structure of the secondary wake. Comparisons with classical approaches show that the contrails generated by this work methodology are wider and more opaque, indicating a potentially greater warming effect.

1 Introduction

Contrails, short for condensation trails, are the long ice clouds visible in the wake of airplanes on clear days. Those anthropogenic clouds result from the nucleation of the water vapor located in the gas mixture between exhaust gases emitted from aircraft engines and cold ambient air. In ice-supersaturated regions of the troposphere, contrails can evolve into cirrus clouds and persist for several hours over hundreds of kilometers before dissipating, thereby increasing regional cloudiness in the meantime. Like any cloud, cirrus clouds induced by contrails interact with both solar and terrestrial infrared radiation, thus impacting Earth's radiative balance. The effect of such artificial clouds on Earth's radiative balance has been quantified in a recent compilation of studies Lee et al. (2021). This work enabled the estimation of contrails' Effective Radiative Forcing (ERF) and other forcing agents such as CO2, NOx, aerosols, and water vapor. The ERF of cirrus clouds induced by contrails has been estimated at 57.4 $\mathrm{mW \cdot m^{-2}}$ which is almost twice as much as the ERF of CO2, estimated at 34.3 $\mathrm{mW \cdot m^{-2}}$.

https://doi.org/10.5194/egusphere-2025-1865
Preprint. Discussion started: 26 May 2025

However, the estimated value of contrails' effective radiative forcing is controversial due to the high uncertainty surrounding this value. This uncertainty primarily reflects the difficulty in accurately estimating the optical properties of contrails, which depend on their microphysical properties (ice crystal concentration, crystal size distribution, etc.), as well as their vertical and horizontal extent. Moreover, the microphysical properties of a contrail several hours old are strongly influenced by these same microphysical properties in the initial moments (see Lewellen and Lewellen (2001); Unterstrasser and Görsch (2014)). During these initial moments, that is, within the first minutes of its lifecycle, the evolution of contrails results from the interaction between wake aerodynamics, plume chemistry, and microphysical processes. This interaction and the underlying physics must be correctly understood to accurately predict contrails' radiative impact.

The formation and evolution of contrails can be divided into four successive regimes (see Gerz et al. (1998); Paoli et al. (2013); Misaka et al. (2015); Jacquin and Garnier (1996)), each governed by specific physical phenomena. The *jet regime*, lasting only a few seconds (see Jacquin and Garnier (1996)), is dominated by strong turbulent diffusion in the engine jet while the wing's vortex sheet rolls into a pair of counter-rotating wingtip vortices. As the jet plume cools down, ice crystals begin to form, making the contrail visible at about one to two wingspans behind the aircraft (see Khou et al. (2015); Ramsay et al. (2024)). In the case of soot-rich emissions, ice crystals primarly form through the condensation of water vapor onto soot particles. Conversely, if soot concentration is low in the plume, ice crystals predominantly form on volatile particles that have formed earlier in the plume, such as sulfuric acid droplets (see Kärcher (1998)). Interaction between the jet and vortices becomes significant around ten wingspans for a typical airliner and can be quantified by looking at the R_3 ratio defined in Jacquin and Garnier (1996).

The *vortex regime* begins when the plume's evolution is dominated by the action of wake vortices, action characterized by the plume roll-up around the wingtip vortices. As time passes, the vortex pair descends due to mutual induction, carrying a significant fraction of the ice crystals downward. This descent results in the adiabatic heating of those crystals and thus to a potential ice crystals sublimation.. However, the vortex pair interacts with atmospheric stratification, generating baroclinic vorticity and a secondary wake that redistributes some ice crystals back to flight altitude and further as observed in Unterstrasser (2014) and where ambient conditions are more favorable for crystals growth. After several tens of seconds, Crow instability, which was theorized in Crow (1970); Crow and Bate Jr (1976), deforms the vortex pair, marking the transition to the dissipation regime. This regime, lasting a few minutes, ends with the destruction of the vortices and the formation of a chain of vortex rings periodically distributed along the flight direction and that can often be observed in the sky on clear days. This marks the beginning of the *diffusion regime*. In this phase, contrail evolution is driven by atmospheric conditions only, including atmospheric turbulence, wind shear, and stratification. If the air remains supersaturated with respect to ice, the contrail may transform into cirrus clouds, potentially persisting for hours. This happens in the so-called ice super-saturated regions (ISSR) that can frequently be found in the tropopause. A significant part of the *diffusion regime* was previously simulated by Paoli et al. (2017) through a 3D temporal LES approach and by Unterstrasser (2014) through a 2D approach.

Simulating a contrail over its entire lifecycle with a satisfactory level of fidelity presents a significant challenge. This is primarily due to the wide range of physical phenomena and scales involved in the four regimes making up the life of a contrail. Directly simulating all the scales of a contrail while accounting for its full spatiotemporal development is currently

https://doi.org/10.5194/egusphere-2025-1865
Preprint. Discussion started: 26 May 2025

prohibitive in terms of computational cost. Nevertheless, understanding the formation and the evolution of a contrail is crucial to developing mitigation techniques, such as the use of sustainable aviation fuels (SAF) or hydrogen fuel that leads to a significant reduction of nucleation sites (see Voigt et al. (2021)). A commonly adopted solution in the literature consists of performing so-called temporal LES for which periodic boundary conditions are prescribed perpendicularly to the flight direction. The temporal development of a contrail in the fixed ground reference frame can then be computed. Such an approach is valid at a distance from the airplane when jet/vortex interaction becomes significant. The problem that arises then is how to initialize such temporal simulations. In most studies in the literature, a proposed solution is to initialize the wake with analytical solutions modeling a pair of vortices and jet plumes. For instance, the vortices are often defined using the Lamb-Oseen solution while turbulence inside the jet is randomly generated with a normal distribution as in Holzäpfel et al. (2001); Paoli et al. (2013); Unterstrasser (2014); Unterstrasser and Görsch (2014); Lewellen and Lewellen (2001). Such an approach simplifies the aircraft wake by idealizing it. Consequently, some aspects of the near-field aerodynamics are neglected, and their potential effect on the far-field is not taken into account. The hypothesis that the effects of the near-field on the far-field can be neglected must be examined. This is all the more important given the increase in geometrical complexity of future aircraft concepts, such as blended wing bodies and rhomboidal wings.

Recently, a methodology has been developed in Bouhafid et al. (2024) in order to simulate the evolution of an aircraft wake from vortex formation, up to their dissipation several minutes later. This methodology was successively used to bridge the gap between the near-field aerodynamics of the jet regime and the far-field aerodynamics of the vortex and dissipation regimes without using analytical solution initialization for the temporal LES of the wake. This allowed us to take into account the full effects of the aircraft geometry on the wake aerodynamics. The same study also compared the wake dynamic when their methodology is used compared to the usual analytical initializations. This comparison has shown significant impact of the horizontal tailplane vortices on the wake evolution and its interaction with the plume.

Therefore, the objective of this work is to apply the methodology developed in Bouhafid et al. (2024) to simulate a contrail from the formation of the first ice crystals to the end of the dissipation regime and to compare the results with the usual analytical initialization in order to see how the differences observed in wake dynamic impact the properties of the contrail in its early life, that is to say before contrail-to-cirrus transition. In addition, the influence of horizontal tailplane vortices on contrails is investigated.

The outline of this paper is as follows. Section 2 describes the methodology and the corresponding numerical framework for simulating a contrail from the jet regime to the dissipation regime. Section 3 gives details about the different simulation setups and the corresponding numerical parameters. Section 4 presents the results of the methodology applied to the NASA Common Research Model (CRM) geometry in cruise flight conditions, geometry representative of Boeing B777 airliner. An examination is conducted regarding the influence of the far-field initialization strategy. Finally, Section 5 concludes this work and highlights its different perspectives.

https://doi.org/10.5194/egusphere-2025-1865
Preprint. Discussion started: 26 May 2025

2 Methodology and numerical framework

2.1 Governing equations

Classical compressible Reynolds-averaged Navier-Stokes (RANS) and compressible Large Eddy Simulation (LES) equations are solved for a multi-species gas mixture using ONERA in-house finite volumes solver CHARME (see Refloch et al. (2011)).

Closing the RANS equations requires a turbulence model to compute the correlation terms. The turbulence model used in this work is the DRSM (Differential Reynolds Stress Modeling) ATAAC model (see Schwamborn and Strelets (2012)) where a transport equation is solved for each of the six Reynolds stresses, with a modelization of the pressure-strain correlation term based on Wilcox's work in Wilcox et al. (1998). Two additional equations are solved: one for the specific dissipation ω and another to model damping for near-wall turbulence. Unlike most two-equations turbulence models, DRSM models do not make the Boussinesq hypothesis, which makes them more accurate for solving strong vortical flows compared to eddy-viscosity models as observed by Churchfield and Blaisdell (2009).

For the LES, subgrid terms are modeled using the Smagorinsky model. In the context of contrail simulation, heat production is due to latent heat release caused by water condensation or sublimation. In practice, this term can be neglected before aerodynamic phenomena for young contrails, as stated by Lewellen and Lewellen (2001) and Unterstrasser (2014). However, it is important to note that latent heat release cannot be neglected for older contrails in the diffusion regime (see Paoli et al. (2017)), which are beyond the scope of this work.

For both RANS and LES equations, convective fluxes are computed using the HLLC scheme with second-order accuracy. A second-order scheme is used for the computation of the diffusive fluxes. Time integration is performed using Backward Euler method for RANS calculations and Implicit Second-Order Runge Kutta for the LES. The GMRES method is used to solve the linear system obtained after the finite volumes discretization of the RANS/LES equations.

2.2 Microphysical model

The microphysical model used for the formation of contrail ice crystals is a simplified version of the bulk model developed by Jean-Charles Khou et al. (see Khou (2016); Khou et al. (2015); Montreuil et al. (2018)). More precisely, the exhaust plume is modeled through a multi-species gas mixture approach and is composed of seven species: dry air, water vapor H_2O, ice H_2O_s, sulfur trioxide SO_3, sulfuric acid H_2SO_4, sulfur trioxide in the adsorbed state $SO_{3,\mathrm{ads}}$ and sulfuric acid in the adsorbed state $H_2SO_{4,\mathrm{ads}}$. A transport equation is solved for the mass fraction Y_i of each species. The corresponding transport equations can be found in Montreuil et al. (2018). Moreover, ice crystal formation is modeled through water vapor condensation done exclusively on soot particles previously activated by sulfur trioxide (SO_3) and sulfuric acid (H_2SO_4) molecules. The approach used by this model is purely Eulerian and as a result, the quantities associated with soot particles, ice crystals, and sulfur species are treated as fields whose values depend on spatial coordinates and time. In the complete version of Khou's model (see Khou (2016)), the formation chemistry of SO_3 and H_2SO_4 molecules is considered through a reaction scheme involving 23 species and 60 reactions. This reaction scheme is not included in this work to reduce computational costs. Instead, it is assumed that SO_3 and H_2SO_4 molecules form very quickly after the engine exhaust gases are emitted, allowing their mass fractions to be

https://doi.org/10.5194/egusphere-2025-1865
Preprint. Discussion started: 26 May 2025

directly prescribed in the engine outlet boundary conditions. This assumption is supported by contrail simulations for similar cases using the complete model performed at ONERA. In sum, the gas mixture contains seven species: air, water vapor H_2O, ice water H_2O_s, sulfur trioxide SO_3, sulfuric acid H_2SO_4, sulfur trioxide in the adsorbed state $SO_{3,\text{ads}}$ and sulfuric acid in the adsorbed state $H_2SO_{4,\text{ads}}$.

Mathematically, the microphysical model first solves a transport equation for the soot density number N_s:

$$\frac{\partial}{\partial t}(\rho N_s) + \frac{\partial}{\partial x_i}(\rho v_i N_s) = \frac{\partial}{\partial x_i}\left(\rho D_{\text{diff}} \frac{\partial N_s}{\partial x_i}\right) \tag{1}$$

Thus, the equation for N_s is the equation of a passive scalar that does not influence flow properties (velocity, pressure, and temperature). D_{diff} is the diffusion coefficient of soot particles for which the corresponding Schmidt number Sc with respect to air kinematic viscosity is set to 1. The turbulent Schmidt number Sc_t for the corresponding RANS and LES equation is set to 0.9. The corresponding LES equation is closed with Smagorinsky model and gradient hypothesis.

Soot activation occurs solely through the adsorption of SO_3 and H_2SO_4 molecules. Two new species are introduced: $SO_{3,\text{ads}}$ and $H_2SO_{4,\text{ads}}$, with their respective mass fractions denoted as $Y_{SO_{3,\text{ads}}}$ and $Y_{H_2SO_{4,\text{ads}}}$. These species represent SO_3 and H_2SO_4 molecules in the "adsorbed" state, as opposed to their "free" state. The transition from "free" to "adsorbed" states occurs through the reactions:

$$SO_3 \rightarrow SO_{3,ads} \tag{2}$$

$$H_2SO_4 \rightarrow H_2SO_{4,ads} \tag{3}$$

We define the activated surface fraction θ_{act} of a soot particle. This quantity is equal to the ratio of the hydrophilic surface area to the total surface area of a given soot particle. A mass conservation equation is solved for the adsorbed species $SO_{3,\text{ads}}$ and $H_2SO_{4,\text{ads}}$. The corresponding source term $\dot{\omega}_{i,\text{ads}}$ is given by:

$$\dot{\omega}_{i,ads} = \frac{\pi D_s^2 \alpha_{ads} \rho Y_i N_s v_{th,i}}{4 M_i}(1 - \theta_{\text{act}}) \tag{4}$$

where $i = \{H_2SO_4, SO_3\}$, M_i the molar mass of species i, $v_{\text{th},i} = \sqrt{\frac{8 k_b T}{\pi m_{\text{mol},i}}}$ the thermal velocity of species i, $m_{\text{mol},i}$ the molecular mass of species i, D_s is the diameter of a spherical dry soot particle, and α_{ads} is the sticking probability, equal to 1 if $T \leq 420$ K and 0 otherwise. D_s is set to 54 nm in all the calculations performed in this work. This value is in the order of magnitude of experimental measurements of soot particles diameter of a turbofan engine (see Petzold and Schröder (1998)). Note that desorption is not accounted for, meaning that adsorbed molecules cannot leave the soot surface. To ensure mass conservation, the source term $-\dot{\omega}_{i,ads}$ is added to H_2SO_4 and SO_3 mass conservation equations.

https://doi.org/10.5194/egusphere-2025-1865
Preprint. Discussion started: 26 May 2025

The fraction θ_{act} is defined as:

$$\theta_{\text{act}} = \sum_{i,ads} \frac{\text{Na}\rho Y_{i,ads}}{\pi D_s^2 N_s \sigma_0 M_i} \tag{5}$$

where Na is Avogadro constant and $\sigma_0 = \frac{4}{\pi (D_{\text{H2SO4}})^2} \approx 5 \times 10^{18}\ \text{m}^{-2}$ is the surface density of active sites, based on the molecular diameter of H_2SO_4.

Contrails ice is modeled by introducing a new species, H_2O_s, representing water in the solid phase formed through heterogeneous nucleation of water vapor on activated soot. The transformation of water vapor to ice and vice-versa is modeled through the reaction:

$$H_2O \leftrightarrow H_2O_s \tag{6}$$

The source term $\dot{\omega}_{\text{ice}}$, representing the mass production rate of ice crystals due to water vapor deposition around soot particles, is given by:

$$\dot{\omega}_{\text{ice}} = D_{\text{con}} \frac{4\pi r_p \theta_{\text{act}} N_s D_{\text{H}_2\text{O}} G_\alpha (r_p) \left(p_v - p_{\text{sol}}^{\text{sat},S} (r_p, T) \right)}{R_{\text{H}_2\text{O}} T} \tag{7}$$

$$D_{\text{con}} = \begin{cases} 1 & \text{if } p_v > p_{liq}^{\text{sat},S} (r_p, T) \text{ or } r_p > r_s \\ 0 & \text{else} \end{cases} \tag{8}$$

$$p^{sat,S} (r_p, T) = \exp\left(\frac{2\sigma M_{\text{H}_2\text{O}}}{R \rho_{\text{H}_2\text{O}} r_p T} \right) p^{\text{sat}} (T) \tag{9}$$

p_v is the partial pressure of water vapor, T is the static temperature, D_{H2O} is the diffusion coefficient of water vapor, σ is the surface tension coefficient of liquid water, $R_{\text{H}_2\text{O}}$ is the specific gas constant for water vapor, and $\rho_{\text{H}_2\text{O}}$ is the density of water in the liquid phase. r_p is the mean radius of ice crystals, locally defined as:

$$r_p^3 = \frac{3}{4\pi} \frac{\rho Y_{\text{H}_2\text{O}_s}}{\rho_{\text{sol}} N_s} + r_s^3 \tag{10}$$

where ρ is the density of the gas mixture, ρ_{sol} is the density of ice (not to be confused with $\rho_{\text{H}_2\text{O}s} = \rho Y_{\text{H}_2\text{O}_s}$ the density of the H_2O_s species in the gas mixture), and $r_s = \frac{1}{2} D_s$ is the radius of a dry soot particle. The saturation vapor pressures with respect to liquid water and ice are given by the semi-empirical formulas from Murphy and Koop (2005) and the density ρ_{sol} is given by Tabazadeh et al. (2000)

https://doi.org/10.5194/egusphere-2025-1865
Preprint. Discussion started: 26 May 2025

G_α is a dimensionless function used to account for cases where the continuum assumption is no longer valid in the immediate vicinity of an ice crystal:

$$G_\alpha(r_p) = \left(\frac{1}{1+\mathrm{Kn}} + \frac{4\mathrm{Kn}}{3} \right)^{-1} \tag{11}$$

where $\mathrm{Kn} = \frac{\lambda_{\mathrm{air}}}{r_p}$ is the Knudsen number, and λ_{air} is the mean free path of an air molecule in the plume.

Several remarks can be made regarding the expression for $\dot{\omega}_{\mathrm{ice}}$. First, the introduction of the multiplier D_{con} prevents water vapor condensation on dry soot when the air is supersaturated with respect to ice but not with respect to liquid water. However, if ice has already formed around the soot, the nucleation process can continue even if the air is no longer saturated with respect to liquid water. Additionally, the sign of the term $p_v - p_{\mathrm{sol}}^{\mathrm{sat},S}$ indicates whether the air is supersaturated with respect to ice or not. In the first case, the source term is positive, and the crystals grow. In the second case, the source term is negative, and the ice crystals sublimate, returning to water vapor. The conservation of the total mass of water is thus ensured by adding the term $-\dot{\omega}_{\mathrm{ice}}$ to the source term of the H_2O species.

2.3 Bridging the gap between the near-field and the far-field

The methodology used to simulate the evolution of a contrail from the formation of the first ice crystals in the near-field to the wingtip vortices destruction in the far-field is the methodology described and validated in the work of Bouhafid et al. (2024). This methodology was used to simulate the CRM geometry aerodynamic wake from the jet regime to the dissipation regime. A microphysical model, described above, is now added to take into account contrail formation and evolution. A diagram of the methodology is shown in Fig.1. The main ideas of the methodology are as follows. A RANS simulation of the jet regime of a realistic airliner geometry is carried out in the airplane reference frame. Anisotropic mesh adaptation techniques are used to ensure a sufficient resolution of the flow and conservation of wake circulation up to twenty wingspans b behind the airplane. Next, a slice perpendicular to the flight direction is extracted from the RANS simulation. This slice is located far enough behind the airliner that jet/vortex interaction becomes important, and axial gradients become negligible before tangential gradients. The slice and its corresponding flow field are then extruded following the flight direction with an extrusion distance equal to one Crow instability wavelength $\lambda_{\mathrm{Crow}} = 8.6 \times \frac{\pi}{4} b$. This extrusion step generates the LES domain for which periodic boundary conditions are prescribed for the boundaries perpendicular to the flight direction. Moreover, the LES computation is now performed in the ground reference frame instead of the aircraft reference frame. Physically speaking, the temporal LES simulation is equivalent to a certain extent to observing the evolution of a contrail portion located inside a region of the sky after an airliner went through it.

In order to transfer the information from RANS turbulence-related fields (Reynolds tensor, dissipation rate) to the LES domain, synthetic turbulence fluctuations noted u'_{MDSRFG} are generated using the MDSRFG method developed in Castro and Paz (2013) and added inside the plume, which is defined for a given position x by the isosurface $U_x > \frac{1}{2}(U_j + U_\infty)$ with U_j the maximum axial velocity in the plume and U_∞ the flight speed. Another synthetic turbulence fluctuation field u'_{atm} is generated in the entirety of the LES domain using the MDSRFG method. This fluctuation field aims to model atmospheric

https://doi.org/10.5194/egusphere-2025-1865
Preprint. Discussion started: 26 May 2025

turbulence responsible for the vortices destruction. The mathematical formulation of the synthetic turbulence is fully described in Bouhafid et al. (2024). Finally, stratification is taken into account by including the effect of gravity in the LES and allowing both ambient static temperature and ambient static pressure to vary with altitude z for a given Brunt-Väisälä frequency N_b.

3 Computational domain and numerical parameters

The methodology described in the previous section is now applied to the NASA Common Research Model geometry to which jet engines were added. First, a RANS calculation of the near-field is carried out and the results are discussed in Section 4.1. Afterward, the RANS calculation is extended to the far-field in Section 4.2 using a temporal LES according to the methodology developed in this work. The RANS and LES computational domains are described below.

3.1 RANS domain

The RANS domain is the same as the one in Bouhafid et al. (2024) and consists of the B777-like CRM geometry inside a box. In terms of design parameters for the CRM geometry, wingspan b is 58.8 m, wing area S is 383 m^2, and mean chord c_m is 6.5 m. The box dimensions are $L_x \times L_y \times L_z$ with $L_x = 30b$, $L_y = 20b$ and $L_z = 20b$ as illustrated in Fig.2.

The distance behind the aircraft in the RANS domain is equal to $20b$. Only half of the aircraft is taken into account in the simulation as the CRM geometry is cut in half by the symmetry plane $y = 0$. This is a common hypothesis justified by the symmetry of the mean flow with respect to the plane $y = 0$.

The contrail is studied for cruise flight conditions with a flight Mach number $M_\infty = 0.85$ and an angle of attack $\alpha = 3°$ (see Tab.1). The ambient static pressure p_∞ and ambient static temperature T_∞ are typical for an altitude of 11 km inside the troposphere. The effect of stratification can be neglected in the jet regime and is thus not taken into account in the RANS

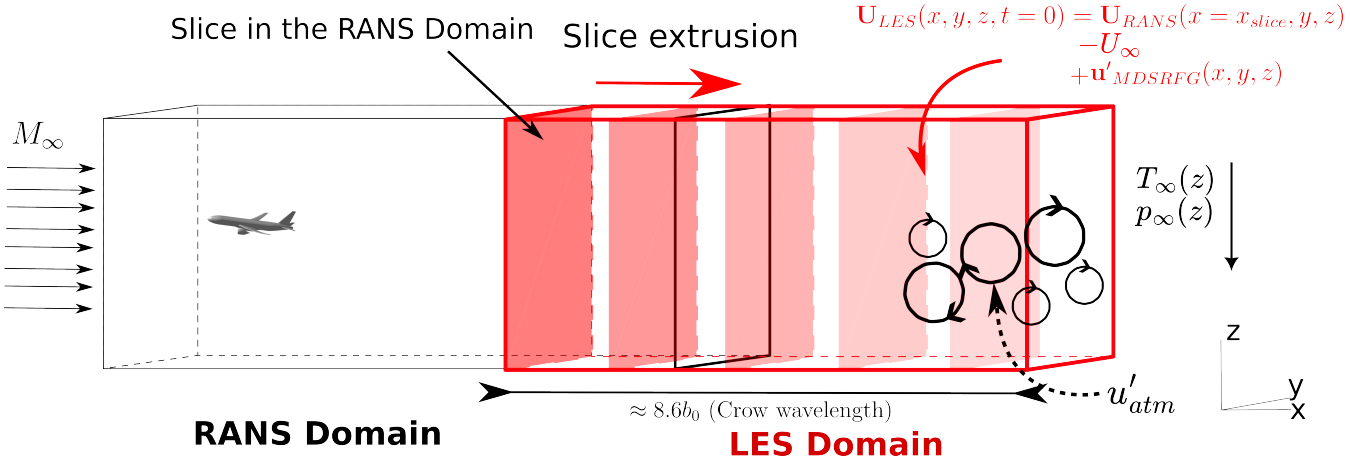

Figure 1. Diagram of the initialization methodology of a far-field calculation using a near-field calculation. (M_∞, U_∞, T_∞ and p_∞ are respectively flight Mach number, flight speed, ambient static temperature and ambient static pressure).

https://doi.org/10.5194/egusphere-2025-1865
Preprint. Discussion started: 26 May 2025

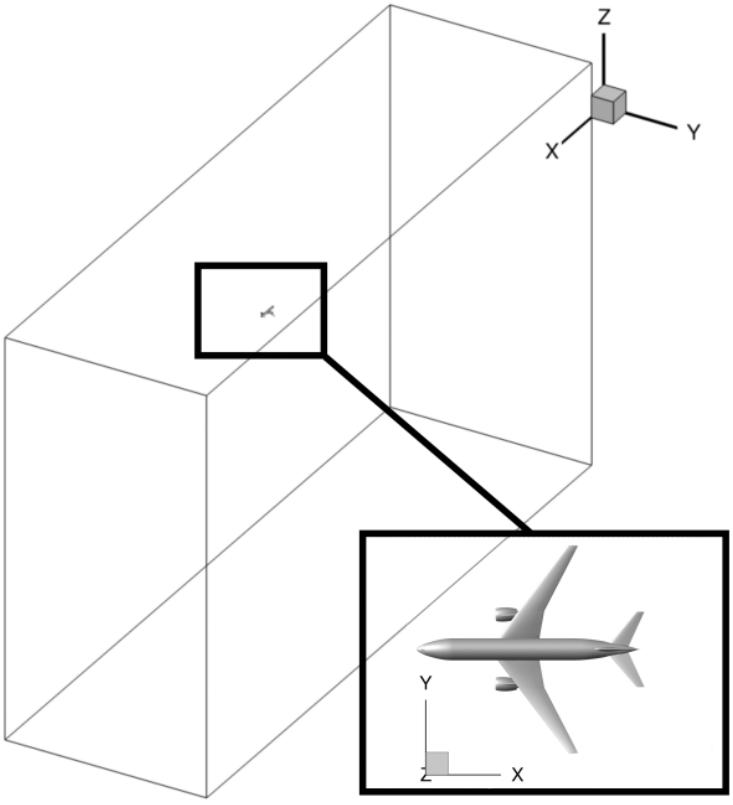

Figure 2. RANS computational domain with the CRM geometry. Only half of the geometry is taken into account in the computational domain.

calculation. Ambient water vapor mass fraction was chosen to impose $RH_{\mathrm{ice}} = 109\ \%$ and $RH_{\mathrm{liq}} = 68\ \%$ (see Tab.**??**), with RH_{ice} and RH_{liq} being respectively the ambient relative humidity with respect to ice and the ambient relative humidity with respect to liquid water.

Turbofan engines were added to the CRM geometry by ONERA, as seen in Fig.3. Their position relative to the wing-tip is $b_j/b = 34\ \%$. The engine inlet and engine outlet are modeled with inlet/outlet boundary conditions (outlet boundary conditions for the engine inlet and inlet boundary conditions for the engine outlet). The thermodynamic values used to define these boundary conditions were chosen to mimic an Ultra-high bypass ratio (UHBR) turobfan while ensuring mass conservation between the inlet and the outlet. The relevant microphysical parameters for the engine outlet are given in Tab.**??** and were chosen to mimic the emissions of a turbofan burning kerosene *Jet A1*. The soot number density at the engine outlet and the dry soot particle radius are of the order of magnitude of previous studies (see Montreuil et al. (2018); Khou et al. (2015); Ramsay et al. (2024)) and is in the same order of magnitude of in-situ measurements performed by Petzold et al. (1999). The water mass vapor at the engine outlet is based on the study of Garnier et al. (1997) and represents the water mass vapor emissions of a B767 equipped with Rolls-Royce RB211 engines.

https://doi.org/10.5194/egusphere-2025-1865
Preprint. Discussion started: 26 May 2025

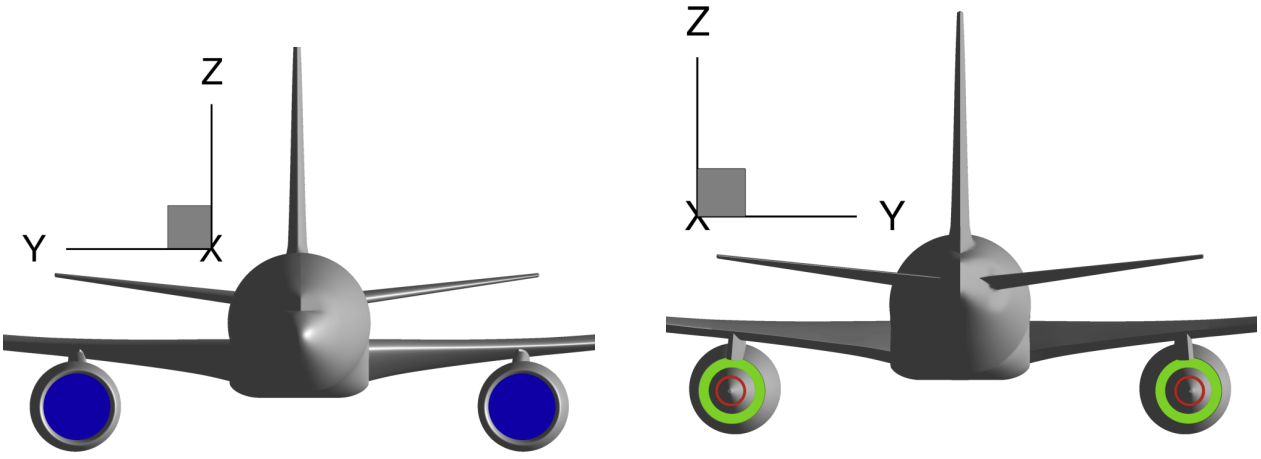

(a) Engine inlet

(b) Core engine outlet & Bypass engine outlet

Figure 3. CRM geometry with jet engines

Atmospheric & engine conditions				
Flight conditions	$\mathbf{M}_\infty$ 0.85	α 3°	$\mathbf{p}_\infty$ 264.37 hPa	$\mathbf{T}_\infty$ 223.15 K
Core engine outlet	**Stagnation temperature** 626.41 K	**Stagnation pressure** 530.01 hPa		
Bypass engine outlet	297.23 K	699.21 hPa		
Engine inlet	$\mathbf{p}$ 370.12 hPa			

Table 1. Atmospheric & engine conditions

The mesh of the RANS domain was generated using an anisotropic mesh adaptation technique based on the total kinetic energy (mean flow kinetic energy + turbulent kinetic energy) field. This was done thanks to the software Feflo.a from INRIA based on Loseille and Alauzet's work (see Loseille and Alauzet (2011a, b)). The final mesh contains around 110 million cells with around 40 million prisms and 70 million tetrahedra. It is the same mesh that was used in Bouhafid et al. (2024) for the study of the near-field aerodynamics of the CRM geometry in cruise flight conditions. Keeping the same mesh is equivalent to assuming that the microphysical processes are not energetic enough to significantly influence the aerodynamic properties of both the vortex wake and the jet.

https://doi.org/10.5194/egusphere-2025-1865
Preprint. Discussion started: 26 May 2025

3.2 LES domain

The LES domain is obtained by extruding along the flight direction x the slice $x/b = 18$ extracted from the RANS calculation as described in Sec.2.3. The extrusion distance is equal to one Crow instability wavelength $\lambda_{\text{Crow}} = 8.6b_0 = 396\ \text{m} \approx 400\ \text{m}$. The LES domain is $20b \approx 1.2\ \text{km}$ long in the y and z direction in order to avoid spurious boundary effects. The LES mesh contains approximately 160 million hexahedral cells, with 100 cells in the flight direction. Such resolution in the axial direction is enough to correctly solve Crow instability but might not be enough if we aim to correctly resolve all short wavelength instabilities that could appear, as stated in Bouhafid et al. (2024). The mesh resolution in the y and z direction is maximum in the zone where the vortices come down because of their mutual induction. The length of the cells was chosen in order to provide 10 points per vortex core radius r_c, i.e. $\text{d}y = \text{d}z \approx 0.1r_c$.

Periodic boundary conditions are imposed for the boundaries perpendicular to the flight direction x while far-field boundary conditions are chosen for the other boundaries where the fluid velocity is equal to 0 and the pressure and temperature fields are imposed to ambient values according to stratification. Temporal integration is performed using Implicit Runge-Kutta 2nd-order method with a time step chosen to verify $CFL < 0.5$, CFL being the Courant number.

The synthetic turbulence in the jet region is generated using a Karman-pao spectrum. The corresponding turbulence dissipation rate ϵ_{jet} and integral length scale are deduced from the RANS calculation and are respectively equal to $50\ \text{m}^2/\text{s}^{-3}$ and $r_j = 6\ \text{m}$, which is the jet radius at $x/b = 18$. The turbulence spectrum is discretized from the integral length scale to the smallest cell length.

Atmospheric conditions in the temporal LES are determined by atmospheric turbulence dissipation rate ϵ_{atm} and Brunt-Väisälä frequency N_b characterizing stratification. Atmospheric turbulence is generated by adding synthetic turbulence fluctuations to the LES initial velocity field. Horizontal and vertical fluctuations are respectively modeled using the horizontal spectrum $E_h = C_k \epsilon_{\text{atm}}^{2/3} k^{-5/3}$ and vertical spectra $E_v = \frac{C_k}{r^2} \epsilon_{\text{atm}}^{2/3} k^{-5/3}$. C_k is the Kolmogorov constant set at 1.5 (see Pope (2001)) and r is the anisotropy factor defined by $r = \frac{u'_h}{u'_v}$ with u'_h and u'_v being respectively the root mean square values of the horizontal and vertical fluctuations of atmospheric turbulence. The two spectra are discretized from $k = k_{\text{Crow}} = \frac{2\pi}{\lambda_{\text{Crow}}}$ to $k = \sqrt{8} k_{\text{Crow}}$. r is set to 5/4 (see Holzäpfel et al. (2001)) and ϵ_{atm} to $6 \times 10^{-5}\ \text{m}^2/\text{s}^{-3}$, a typical value in the upper troposphere as measured in Cho and Lindborg (2001). The correspond turbulent time scale is $\tau_b = \left(\frac{\lambda_{\text{Crow}}^2}{\epsilon_{\text{atm}}} \right)^{1/3}$. For the CRM geometry and the given value of ϵ_{atm}, $\tau_b \approx 23$ min. Since the dissipation regime lasts only a few minutes, it is not necessary to force atmospheric turbulence to avoid turbulence decay.

Concerning stratification, two Brunt-Väisälä frequencies are considered in this work: $N_b = 0.012\ \text{s}^{-1}$ and $N_b = 0.03\ \text{s}^{-1}$. The first case corresponds to a standard value for medium stratification while the second case corresponds to a strong stratification scenario. These values are consistent with previous observations made in Schumann et al. (2017). Knowing the value of N_b, the vertical profile for ambient pressure and ambient temperature can be deduced by the equations:

$$\frac{N_b^2}{g} = \frac{1}{\Theta_\infty} \frac{\text{d}\Theta_\infty}{\text{d}z} \tag{12}$$

https://doi.org/10.5194/egusphere-2025-1865
Preprint. Discussion started: 26 May 2025

$$\frac{\mathrm{d}p_\infty}{\mathrm{d}z} = -\rho_\infty(z)g \tag{13}$$

where Θ_∞ is ambient potential temperature, g is gravitational acceleration, and ρ_∞ ambient air density. The solution equations can be found in Paoli et al. (2013). Solving those equations for the case $N_b = 0.03\ \mathrm{s}^{-1}$ with the chosen ambient pressure and ambient temperature at flight altitude gives rise to a temperature inversion phenomenon. That is to say, the temperature decreases when altitude decreases instead of increasing as observed for $N_b = 0.012\ \mathrm{s}^{-1}$. This gives rise to an increase in relative humidity when altitude decreases. Temperature inversion layers in the tropopause were already observed in the past, and their characteristics were examined in previous works (see Birner (2006); Grise et al. (2010)).

4 Results and discussion

The results of the contrail simulations from the near-field to the far-field are discussed in this section for the two stratification scenarios. In order to evaluate the impact of the temporal LES initialization strategy, another contrail simulation of the far field is carried out using the classical analytic initialization strategy commonly used in literature, where the vortices are idealized by a pair of two Lamb-Oseen vortices as in Unterstrasser and Görsch (2014); Unterstrasser (2014); Holzäpfel et al. (2001); Paoli et al. (2013). A comparison is made between the RANS initialization strategy and the analytic initialization strategy. Explanations are given to understand the observed differences. In light of the obtained results, a final simulation is performed using an analytic initialization strategy with four Lamb-Oseen vortices, two for the main wing-tip vortices and two for the horizontal tailplane vortices. All the analysis made below concerns mainly the contrail evolution and its associated microphysics fields since the analysis of the aerodynamic fields was already done in Bouhafid et al. (2024).

4.1 Evolution of the contrail in the near-field

The contrail in the near-field can be visualized in Fig.4 where the cells satisfying the condition $\theta > 0.01$, $N_s > 10^7\ \mathrm{m}^{-3}$ and $r_p > 1.5 r_s$ are blanked. For those conditions and the given atmospheric conditions, the contrail appears at around one wingspan behind the engines as seen in Fig.4b. Moreover, Fig.4a allows us to observe the jet deviation caused by the wing-tip vortex, a deviation that is followed by the beginning of the jet roll-up around the vortex.

In order to quantify the evolution of the contrail in the near-field, the relevant microphysical quantities are averaged in a cross-section of the contrail for a given position x. The contrail is identified by the cells satisfying the condition $r_p > r_s$ and the average is weighed by the local number of ice crystals in a given cell. The averaged microphysics quantities are plotted in Fig.5. Fig.5a displays the evolution of the average soot number density as a function of x/b. It can be observed that the dilution of the plume reduces soot number density by two orders of magnitude by the end of the jet regime. The dilution is faster for the first few wingspans because of the jet strong turbulent diffusion. As turbulence inside the plume decreases when

https://doi.org/10.5194/egusphere-2025-1865
Preprint. Discussion started: 26 May 2025

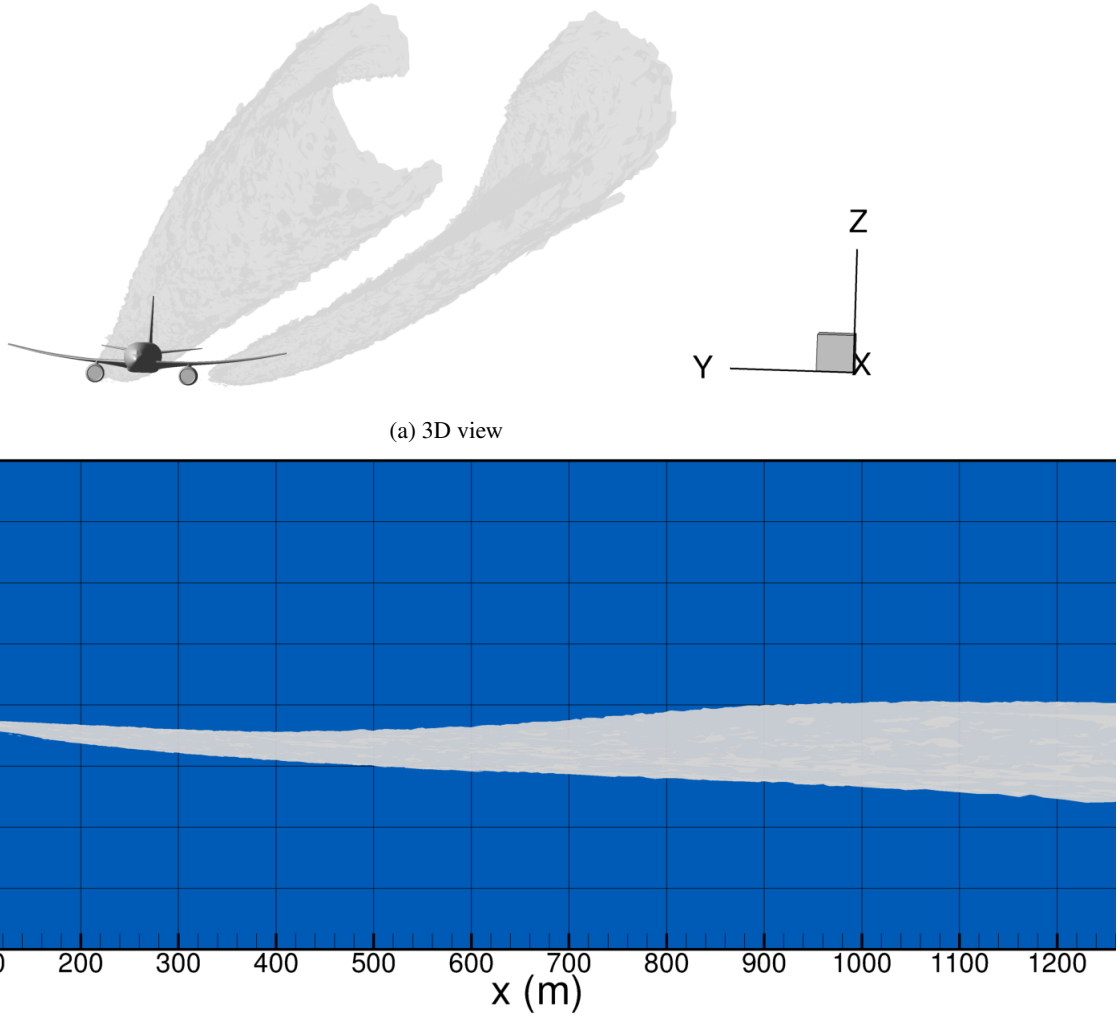

(a) 3D view

(b) $z - x$ view

Figure 4. Mesh cells satisfying $\theta > 0.01$, $N_s > 10^7$ m^{-3} and $r_p > 1.5 r_s$

the distance behind the aircraft increases, dilution becomes slower, and the influence of the vortex on plume dilution becomes more important than turbulent diffusion.

The evolution of the average ice water content (IWC) plotted in Fig.5b can be divided into three zones. First, the IWC evolution shows a sharp growth for the first few wingspans, with an increase equal to four orders of magnitude compared to $x/b = 0.5$. This strong ice production results from the condensation of the excess water vapor present in important quantities in the plume in the early stage of the jet regime. This can be seen too in Fig.5e where relative humidity strongly increases for

https://doi.org/10.5194/egusphere-2025-1865
Preprint. Discussion started: 26 May 2025

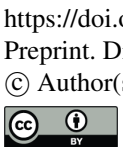

the first three wingspans. Second, for x/b between 5 and 15, the evolution of IWC is no longer monotonous as two maxima appear for $x/b = 4.5$ and $x/b = 11$. This can be explained by the fact that the evolution of IWC results from the competition between two phenomena: ice water dilution and ice water production. Indeed, when plume dilution is greater than ice water production, IWC will decrease and vice-versa when plume dilution is smaller. For the first three wingspans, the effect of ice

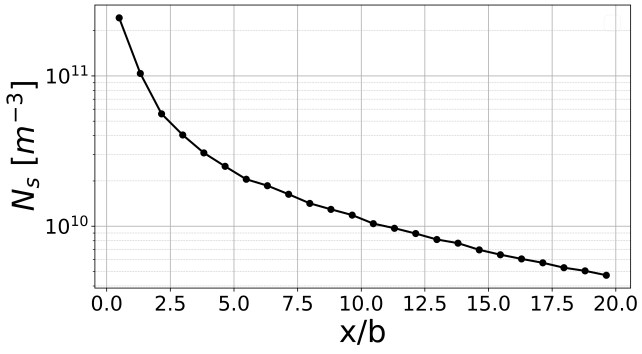

(a) soot number density

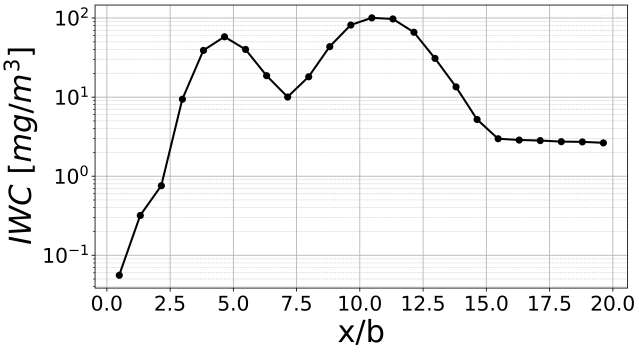

(b) Ice water content

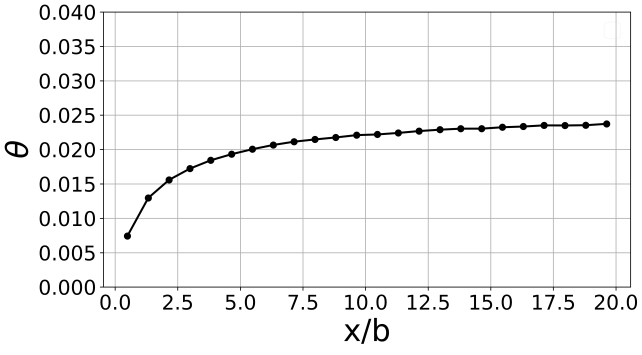

(c) Activated surface fraction

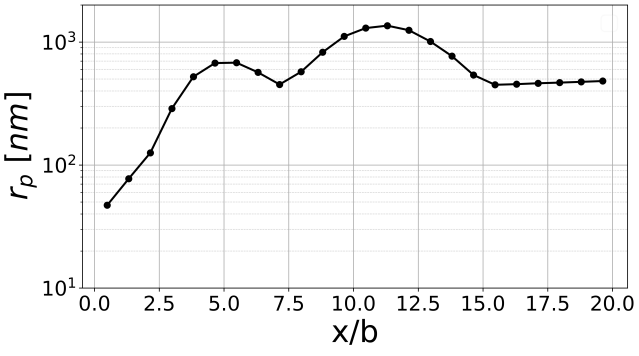

(d) Mean crystal radius

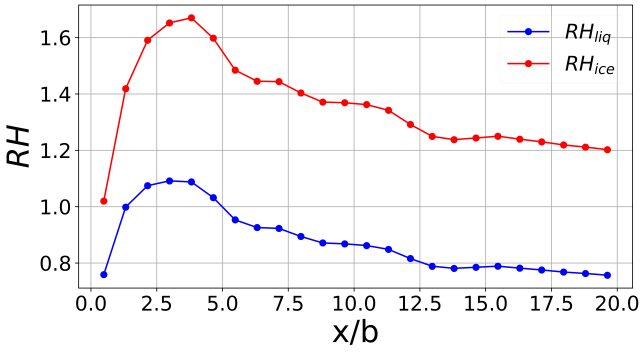

(e) Relative humidity with respect to ice water and liquid water

Figure 5. Microphysical quantities averaged in a cross-section of the plume as a function of the distance behind the aircraft x

https://doi.org/10.5194/egusphere-2025-1865
Preprint. Discussion started: 26 May 2025

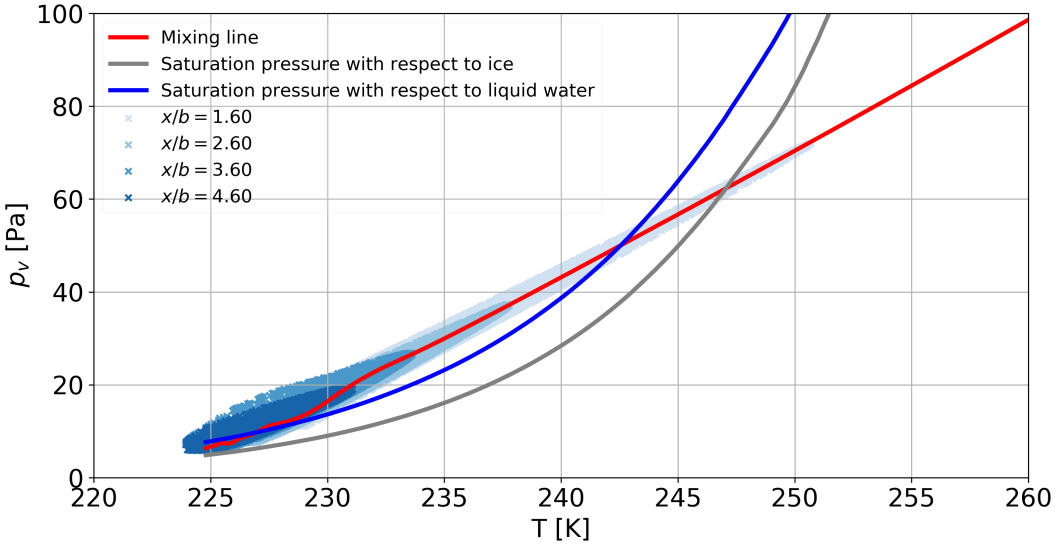

Figure 6. Mixing line of the plume in the near-field plotted in a (p_v, T) diagram. The plume is obtained by averaging fluid variables on thirty streamlines passing through the engine core flow.

water production is superior to the effect of dilution because of the important quantity of excess water vapor in the plume. However, looking at Fig.5e, relative humidity reaches a maximum at $x/b = 3$, that is to say, shortly before IWC does. This results in a decrease in ice water production. Finally, for $x/b > 15$, the value of IWC reaches a plateau that can be interpreted as an equilibrium between ice water dilution and ice water production.

Fig.5c plots the evolution of the averaged activated surface fraction θ_{act}. It appears that soot activation occurs very quickly after the exhaust gases are ejected from the engine. An asymptotic value $\theta_{\text{act}} \approx 2.5\ \%$ is reached at the end of the calculation domain. The existence of an asymptotic value was already observed in Khou (2016) and Kärcher 1D model developed in Kärcher (1998). This was explained by the effect of dilution on sulfur species and the absence of desorption in the used model, meaning that the activated surface fraction of a soot particle cannot decrease.

Regarding the evolution of the averaged mean ice crystal radius r_p plotted in Fig.5d, we can make the same observations and analysis as the ones made for IWC. Indeed, since $r_p \propto \sqrt[3]{\text{IWC}}$, the evolution of r_p will closely follow the evolution of IWC. At the end of the domain, r_p reaches an asymptotic value equal to $500\ \text{nm}$. This value is of the same order of magnitude compared to values obtained in previous similar studies (see Khou et al. (2015); Ramsay et al. (2024); Paoli et al. (2013)). Note that the exact value will strongly depend on the ambient relative humidity, soot number density at the engine exit, and soot activation in the plume. Indeed, the work done by Ramsay et al. (2024) used a very similar microphysical model and assumed that every soot is activated, which explains to some extent why the ice crystals obtained in their simulations are larger compared to this work's.

https://doi.org/10.5194/egusphere-2025-1865
Preprint. Discussion started: 26 May 2025

The mixing line of the plume is plotted in Fig.6 in (p_v, T) diagram, where p_v is the water vapor pressure and T is the temperature. This line is obtained by averaging fluid variables over twenty streamlines originating from the engine core outlet. As the plume ages, both temperature and water vapor pressure decrease due to dilution with the cold ambient air. When the mixing line goes above the saturation pressure curve for liquid water, ice crystals begin to form. These crystals will grow as long as the mixing line remains above the saturation pressure curve for ice, which occurs at approximately $T = 243$ K for the flight conditions considered.

To examine the distribution of (p_v, T) within the plume, the (p_v, T) values in every cell within the plume region — defined as those where $N_s > 0.1 N_{s,\max}$, with $N_{s,\max}$ being the maximum N_s value at a given position x — are plotted for various positions x downstream of the aircraft. The obtained scatterplot provides a clear visualization of how temperature and water vapor pressure vary within the plume for a given plume age. Notably, the older the plume, the less scattered the points become, reflecting the increasing uniformity caused by plume dilution. Finally, we observe that the mixing line differs from a straight line for $T < 230$ K as p_v decreases more abruptly. This is most likely due to the effect of water vapor condensation which decreases p_v more rapidly than the plume isobaric mixing.

4.2 Evolution of the contrail in the far-field

The results of four contrail far-field LES simulations are analyzed and discussed in this subsection. The first two simulations are initialized using the near-field RANS simulation. The other two simulations are initialized using an analytic initialization strategy which proceeds as follows. A vortex pair is initialized with two Lamb-Oseen vortices located at the same position as the RANS vortex pair. The velocity inside the vortices is purely tangential and is defined by:

$$V_{\theta,\mathrm{LO}}(r) = \frac{\Gamma}{2\pi r}\left(1 - e^{-\beta\frac{r^2}{r_c^2}}\right) \tag{14}$$

$$\frac{\mathrm{d}p_{\mathrm{LO}}}{\mathrm{d}r} = \rho\frac{V_{\theta,\mathrm{LO}}}{r} \tag{15}$$

with $V_{\theta,\mathrm{LO}}$ is the tangential velocity, r the radial coordinate defined from the center of the vortex, Γ the vortex circulation, r_c the vortex core radius, p_{LO} the static pressure inside the vortex and $\beta \approx 1.256$. r_c and Γ are deduced from the RANS calculation at $x/b = 18$. The plume is modeled by adding two circular jets with purely axial flow and located at the position of the jet engines in the CRM geometry. The radius of the jet is obtained from the RANS calculation as it was done in Bouhafid et al. (2024). All the flow field variables are uniform inside the jet, with a hyperbolic tangent decrease outside the jets. The value of the flow field variables in the jets is deduced from the RANS calculation. Moreover, the parameters of the hyperbolic tangent decrease are calibrated for the mass fraction fields in order for the total mass of each species to be identical to the total mass obtained from the RANS initialization. The analytic initialization strategy with two Lamb-Oseen vortices will be noted 2LO from now

https://doi.org/10.5194/egusphere-2025-1865
Preprint. Discussion started: 26 May 2025

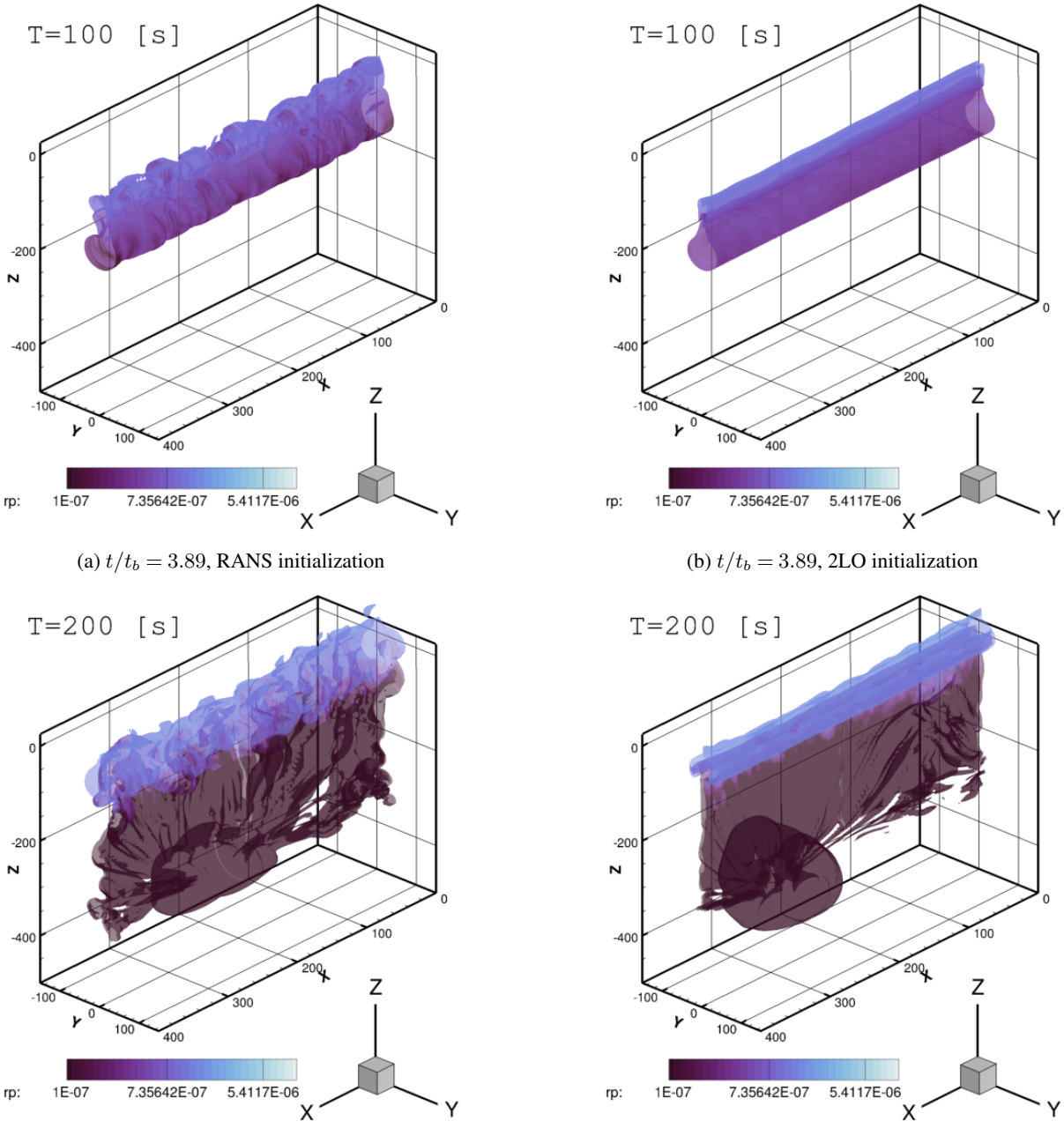

(a) $t/t_b = 3.89$, RANS initialization

(b) $t/t_b = 3.89$, 2LO initialization

(c) $t/t_b = 7.78$, RANS initialization

(d) $t/t_b = 7.78$, 2LO initialization

Figure 7. Soot number density isosurface $N_s = 10^7$ m^{-3} colored by mean crystal radius r_p (m) for $N_b = 0.012$ s^{-1} (medium stratification). Comparison between RANS initialization strategy and 2LO initialization strategy. Distances are in meters.

on. Finally, time is scaled by the vortex pair characteristic time $t_b = \frac{2\pi b_0^2}{\Gamma} = 25.7$ s, which is the theoretical time for the vortex pair to descend a distance equal to b_0 as a result of their mutual induction.

https://doi.org/10.5194/egusphere-2025-1865
Preprint. Discussion started: 26 May 2025

Fig.7 shows at $t/t_b = 3.89$ and $t/t_b = 7.78$ the soot number density isosurface $N_s = 10^7$ m^{-3} colored by mean crystal radius r_p for the medium stratification scenario $N_b = 0.012$ s^{-1}. The important differences regarding the aerodynamic field observed and explained in Bouhafid et al. (2024) between the 2LO initialization and RANS initialization significantly impact the contrail shape and properties. While there are some similarities between the two cases, like the formation of a vortex ring following Crow instability, the contrail in the 2LO case appears much smoother. Conversely, the turbulent nature of the secondary wake in the RANS initialization case originating from short-wave vortex instabilities gives the contrail a more chaotic appearance, while increasing the size of the contrail at flight altitude.

The differences between the 2LO initialization case and RANS case are even greater for the strong stratification scenario $N_b = 0.03$ s^{-1} for which the same soot number density isosurface is plotted in Fig.8 at $t/t_b = 3.89$ and $t/t_b = 7.78$. As expected, more ice crystals are found in the secondary wake for the two initialization strategies compared to the medium stratification scenario. Since atmospheric conditions are favorable for contrail formation in the strong stratification scenario because of thermal inversion, the resulting contrail will contain a higher ice water content and larger crystals. However, we observe that the contrail goes significantly lower in the 2LO case. This results in a wider contrail for the RANS case. A possible explanation for this phenomenon could be that the vortices are more unstable in the RANS case and are destroyed sooner, thus preventing the vortices from going downwards and carrying ice crystals to lower altitudes. The unstable nature of the wake can be amplified either by the development of Windall instability in the RANS initialization—manifesting under certain conditions but absent in the 2LO initialization computation—or by the presence of horizontal tailplane vortices, resulting in a four-vortex system. This will be further examined in Section 4.3.

The differences observed can be quantified by spatially averaging the contrail along flight direction x, with the cells in the contrail being identified by $r_p > r_s$. Fig.9 displays the relevant contrail lengthcales for the RANS initialization and 2LO initialization cases. Contrail height Δz, contrail width Δy, and contrail cross-section A_p area are plotted versus scaled time t/t_b. Contrail height Δz is computed by taking the difference between the maximum value of z and the minimum value of z in the contrail. Contrail width is computed the same way but with the y coordinate. Contrail cross-section area is calculated by summing the area of every cell inside the contrail.

Regarding contrail height, the differences between the RANS initialization and 2LO initialization remain small for the medium stratification scenario. However, for the strong stratification scenario, the contrail is 1.6 times taller for the 2LO initialization case compared to the RANS initialization case. The differences between the four different cases are larger for the contrail width. For both stratification scenarios, the contrail is two times wider for the RANS initialization compared to the equivalent 2LO initialization. For contrail cross-section area, two observations can be made. First, for the RANS initialization, the influence of stratification becomes visible at $t/t_b = 2.5$ while it happens later for the 2LO initialization, at around $t/t_b = 3.5$. Second, the contrail is bigger and grows more rapidly for the strong stratification scenario. This is simply due to the higher ambient relative humidity RH for $N_b = 0.03$ s^{-1} resulting from thermal inversion. For $N_b = 0.012$ s^{-1}, RH eventually decreases below 100% as the vortices descent, resulting in ice water sublimation and contrail surface reduction at $t/t_b = 4.3$. Nonetheless, the contrail begins to grow again at later times because of the ice crystals in the secondary wake ascending back to flight altitude where air is supersaturated with respect to ice water.

https://doi.org/10.5194/egusphere-2025-1865
Preprint. Discussion started: 26 May 2025

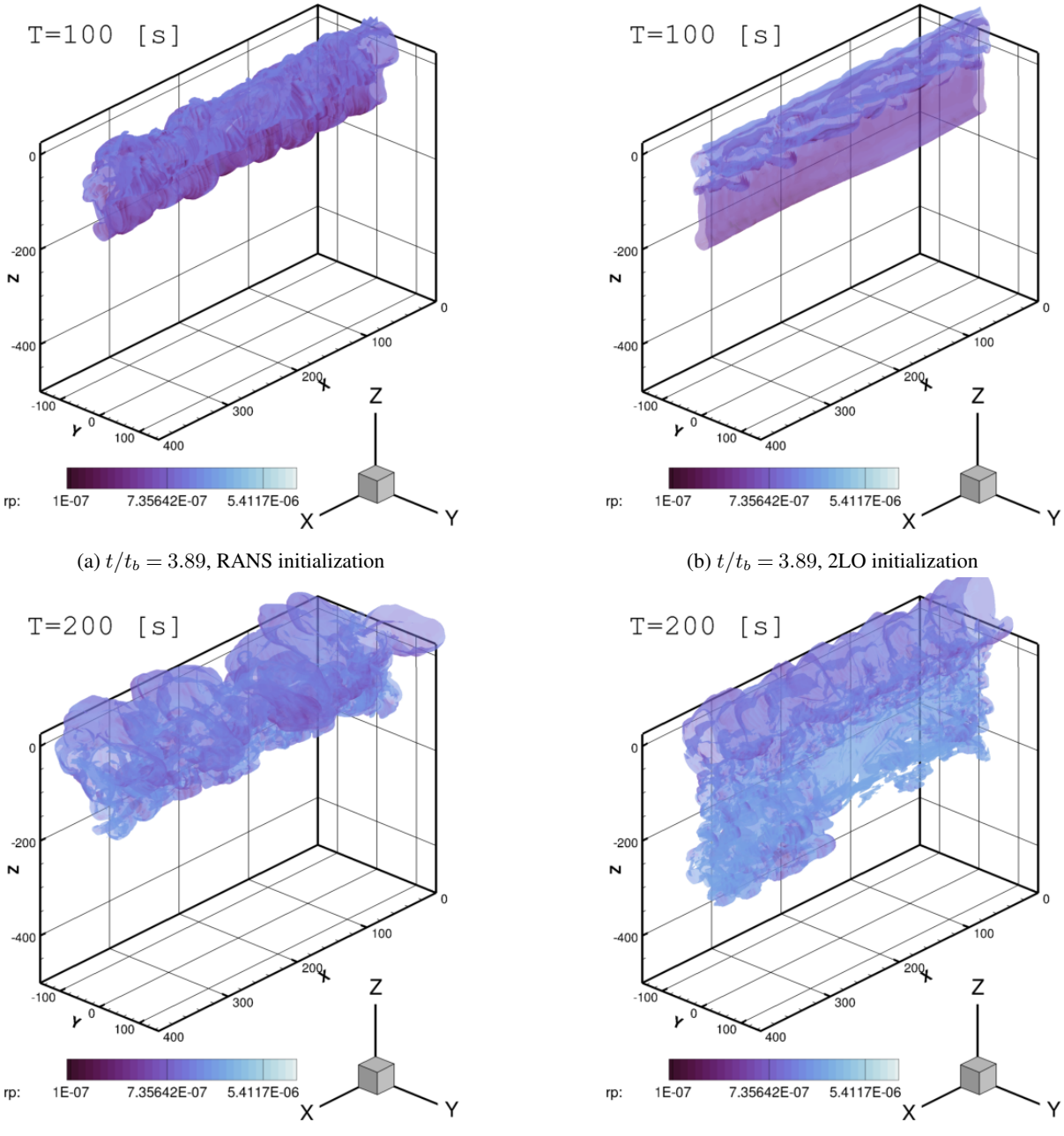

(a) $t/t_b = 3.89$, RANS initialization

(b) $t/t_b = 3.89$, 2LO initialization

(c) $t/t_b = 7.78$, RANS initialization

(d) $t/t_b = 7.78$, 2LO initialization

Figure 8. Soot number density isosurface $N_s = 10^7$ m^{-3} colored by mean crystal radius r_p (m) for $N_b = 0.03$ s^{-1} (strong stratification). Comparison between RANS initialization strategy and 2LO initialization strategy. Distances are in meters.

Microphysical quantities are now averaged inside the contrail cross-section at every time t. Their evolution as a function of t/t_b is plotted in Fig.10. Fig.10a shows soot number density evolution, which decreases about one order of magnitude between

https://doi.org/10.5194/egusphere-2025-1865
Preprint. Discussion started: 26 May 2025

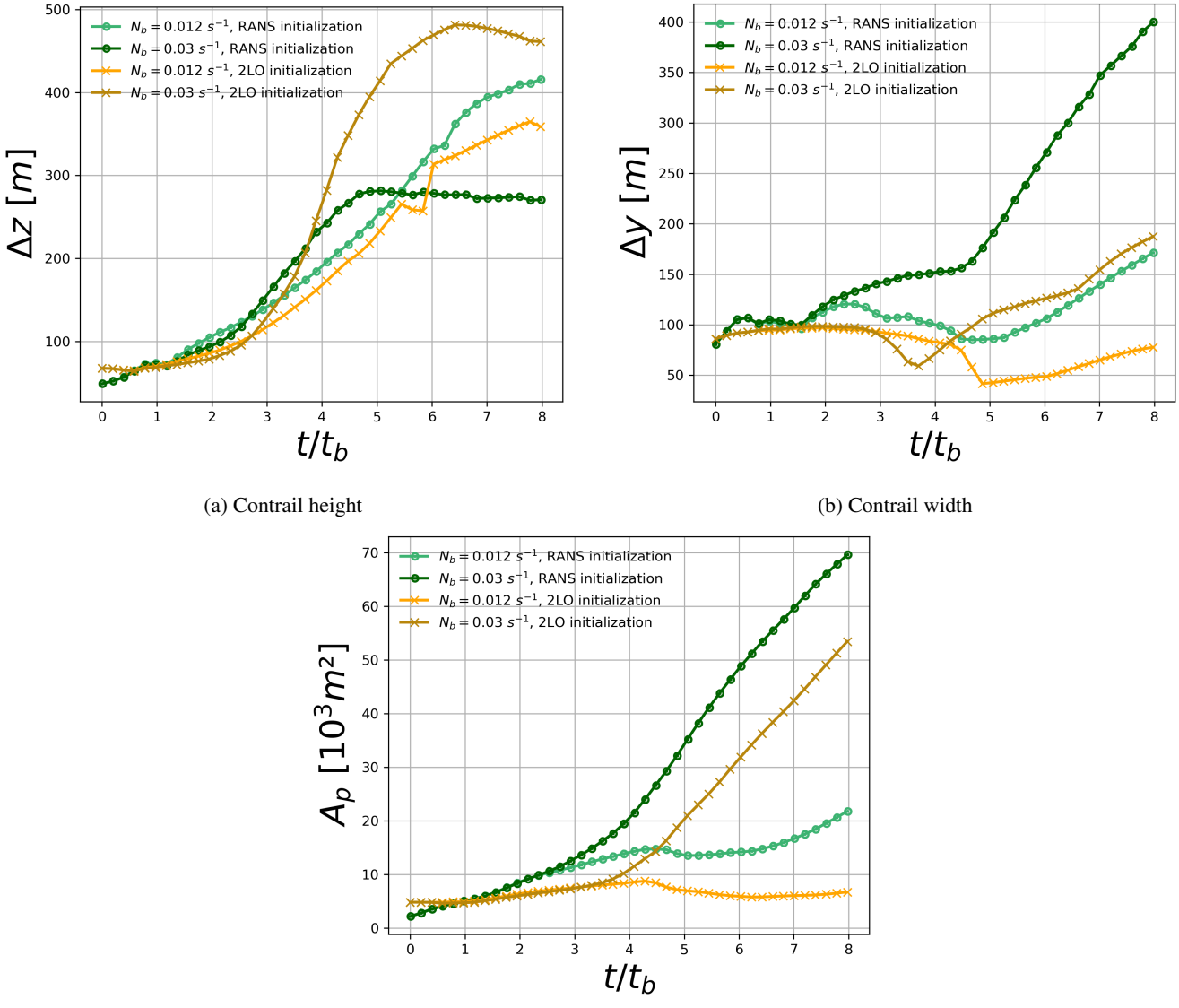

(a) Contrail height

(b) Contrail width

(c) Area of contrail cross-section

Figure 9. Contrail length scales for the different stratification scenarios. Comparison between the 2LO initialization strategy and the RANS initialization strategy.

the beginning of the vortex regime and the end of the dissipation regime for all cases. The smallest decrease is obtained for the 2LO initialization case in the medium stratification scenario. This is due to the smooth and weakly turbulent nature of the secondary wake compared to the RANS initialization, resulting in less mixing of the plume with the ambient air.

Fig.10b displays the evolution of the ice crystal radius. For the medium stratification scenario, r_p begins to increase because the plume is still located in supersaturated air with respect to ice. However, as the plume descends with the vortex pair, the plume

https://doi.org/10.5194/egusphere-2025-1865
Preprint. Discussion started: 26 May 2025

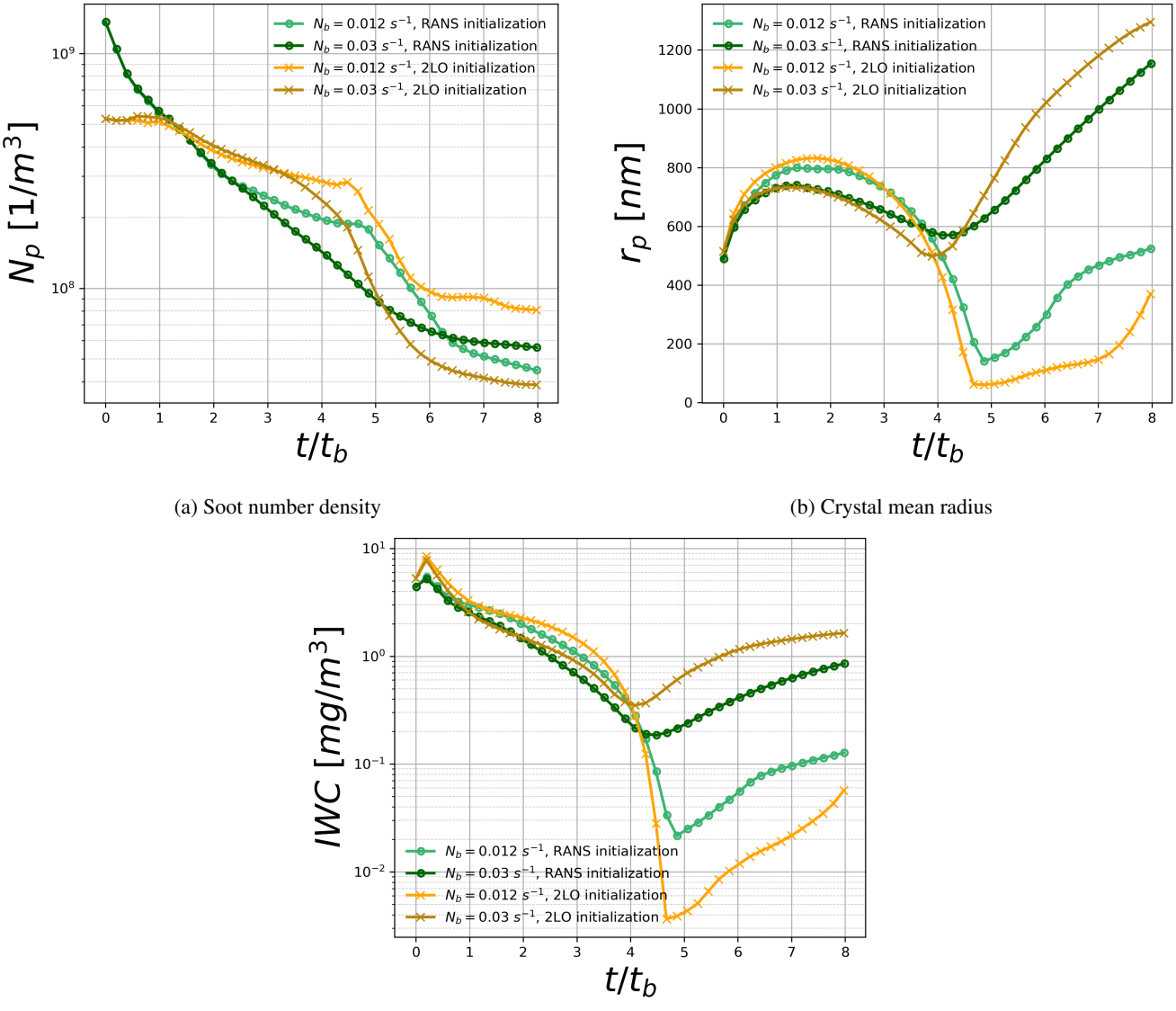

(a) Soot number density

(b) Crystal mean radius

(c) Ice water content

Figure 10. Average contrail microphysics quantities for the different stratification scenarios. Comparison between the RANS initialization strategy and the 2LO initialization strategy.

405 is no longer supersaturated and the crystals begin to shrink. Eventually, every ice crystal in the primary wake is transformed back to water vapor while the crystals in the secondary wake return to flight altitude where they can grow. This results in an increase of the averaged value of r_p in the contrail. Contrastingly, for the strong stratification scenario, the temporary decrease is this time due to some ice crystals quickly moving back to flight altitude and beyond, where the ambient air is not supersaturated in the case of a thermal inversion phenomenon. Eventually, since most ice crystals are trapped in the primary

https://doi.org/10.5194/egusphere-2025-1865
Preprint. Discussion started: 26 May 2025

wake, ice crystals begin to grow as the air becomes more supersaturated as altitude decreases. These explanations also apply to the evolution of the IWC plotted in Fig.10c, with the additional effect of plume dilution.

The overall radiative impact for early contrails can be quantified by computing the extinction E. To do so, we have to compute the optical depth τ_v defined as $I_{\text{tr}} = Ie^{-\tau_v}$ with I the intensity of an incident wave and I_{tr} the intensity of the corresponding transmitted wave after traveling inside the contrail. τ_v is given by Hulst and van de Hulst (1981):

$$\tau_v(x,y) = \int_{-\infty}^{+\infty} \pi r_p^2 N_s Q_{ext}(r_p) dz \tag{16}$$

$$Q_{ext} = 2 - \frac{4}{e}\left(\sin(e) - \frac{1-\cos(e)}{e}\right) \tag{17}$$

with

$$e = \frac{4\pi r_p(\mu_r - 1)}{\lambda} \tag{18}$$

where Q_{ext} is the Mie extinction coefficient. $\mu_r = 1.31$ is the refractive index of ice and λ the wavelength of the incident light wave coming perpendicularly to the contrail. Extinction is then defined by:

$$E(x) = \int_{-\infty}^{+\infty} \left(1 - e^{-\tau_v}\right) dy \tag{19}$$

Physically speaking, the higher is $E(x)$, the more opaque the contrail will appear to an observer located perpendicularly to it, meaning that the contrail will absorb and diffuse more light. Thus, E and τ_v are directly linked to the radiative forcing of contrails.

$E(x)$ is averaged along x for different times t and is plotted in Fig.11 for the two stratification scenarios and the RANS/2LO initializations. We observe that for both stratification scenarios, the highest extinction is obtained for the RANS initialization case. The relative gap between the RANS initialization and the 2LO initialization is maximum for the medium stratification scenario. These differences can be explained by the soot number density, ice crystal radius and contrail size differences that were observed and analyzed previously. We hypothesized above that the vortex pair is more unstable for the RANS initialization in the strong stratification scenario. We can observe that this results in a higher extinction compared to the 2LO initialization. This result is consistent with Ferreira et al. (2024) findings where it was shown that forcing Crow instability, and thus decreasing the lifetime of the wingtip vortices, increased the radiative forcing of young contrails.

It is important to note that extinction is the same at $t = 0$ for every case. Thus, this shows the significant influence of near-field aerodynamics on the contrail evolution in the far-field. Initializing a temporal LES of the far-field with two Lamb-Oseen

https://doi.org/10.5194/egusphere-2025-1865
Preprint. Discussion started: 26 May 2025

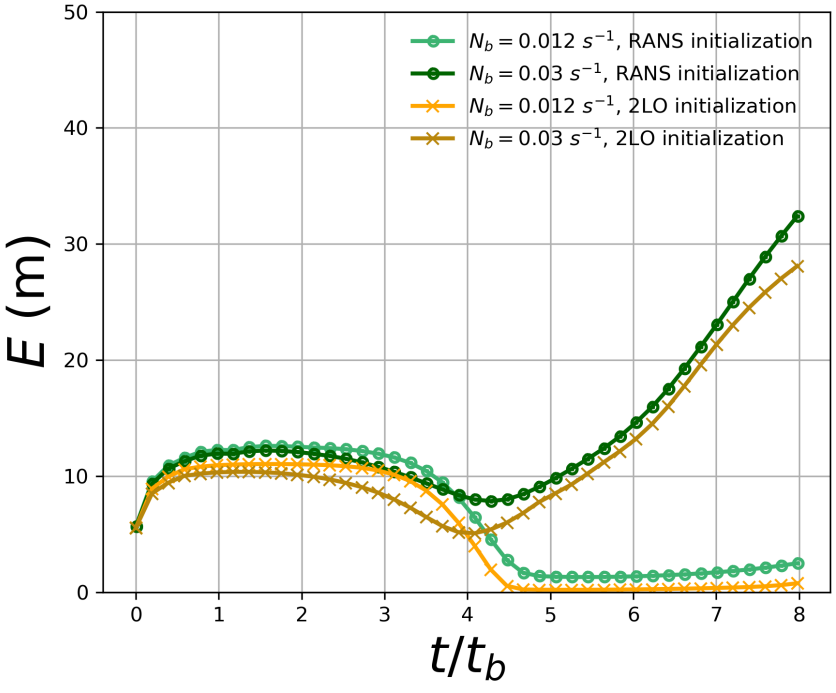

Figure 11. Average extinction as a function of time t for the different stratification scenarios. Comparison between the RANS initialization strategy and the 2LO initialization strategy.

vortices might result in underestimating the radiative impact of young contrails. It would be interesting to use Paoli et al. (2017) methodology to extend the calculation to the diffusion regime and see if the differences persist after an hour.

4.3 Analytic initialization strategy with HTP vortices

In order to better understand the interaction between stratification and short wavelength vortex instabilities, another temporal LES simulation is performed for the medium stratification scenario $N_b = 0.012\,\mathrm{s}^{-1}$. This new simulation is similar to the 2LO initialization strategy. The only difference is that the vortex wake is now initialized with four vortices instead of two. To do so, a new Lamb-Oseen vortex pair is added and aims to model horizontal tailplane (HTP) vortices. The circulation, location and core radius of the HTP vortices are deduced from the RANS calculation and are respectively equal to $-77\ \mathrm{m}^2/\mathrm{s}$ and $2.5\ \mathrm{m}$. This new simulation will now be referred to as 4LO.

Fig.12 shows for $t/t_b = 3.89$ and $t/t_b = 7.78$ a soot number density isosurface colored by ice crystal mean radius for the RANS initialization and 4LO initialization. We observe that the contrail obtained with the 4LO initialization is qualitatively much more similar to the one obtained with the RANS initialization than the one obtained with the 2LO initialization. Indeed, the contrail exhibits the same turbulent aspect, both in the primary and secondary wake. This can be understood by looking at Fig.13, where a Q-criterion isosurface is plotted at $t/t_b = 3.89$ for both cases to visualize the two vortex tubes of the vortex

https://doi.org/10.5194/egusphere-2025-1865
Preprint. Discussion started: 26 May 2025

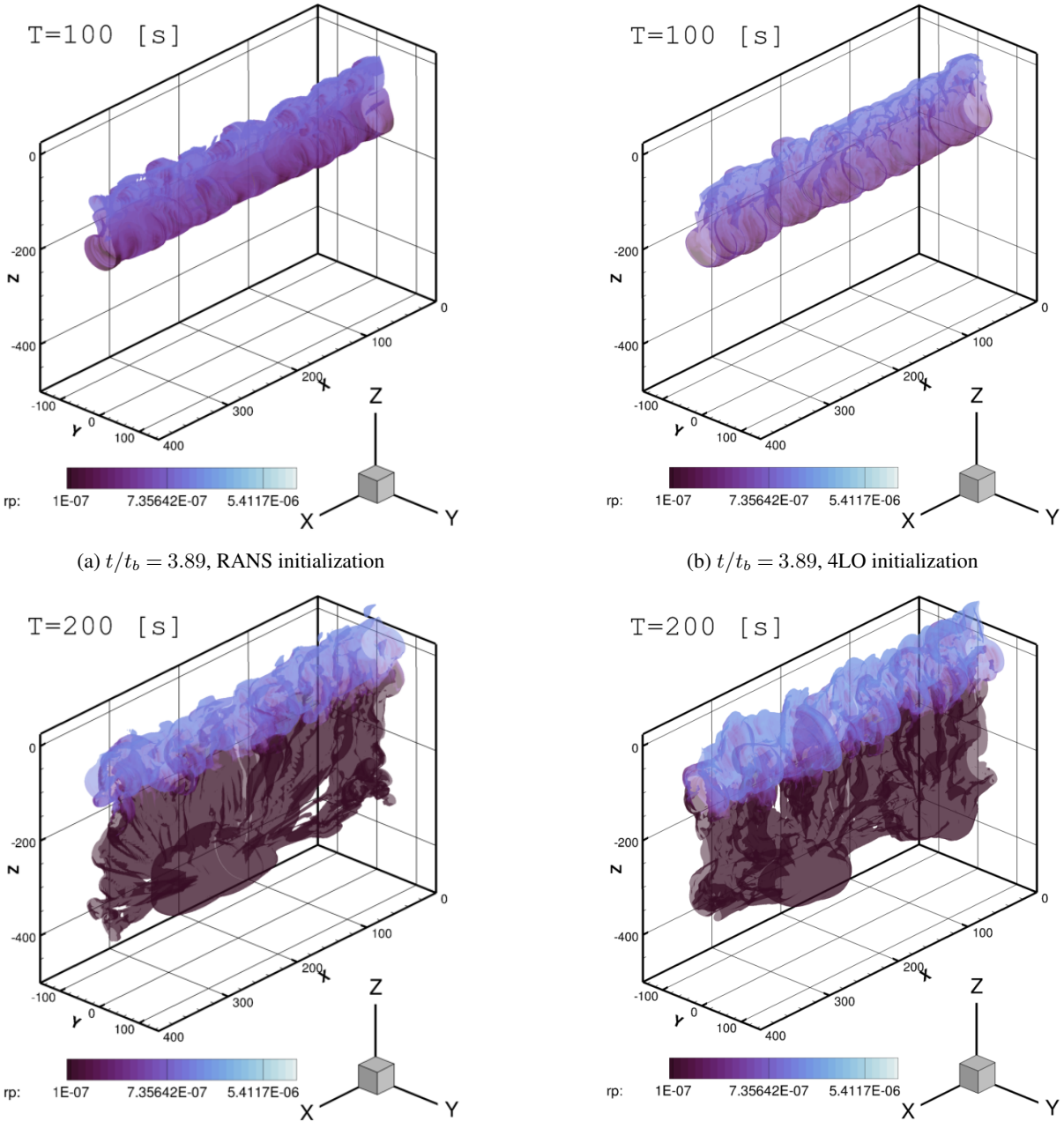

(a) $t/t_b = 3.89$, RANS initialization

(b) $t/t_b = 3.89$, 4LO initialization

(c) $t/t_b = 7.78$, RANS initialization

(d) $t/t_b = 7.78$, 4LO initialization

Figure 12. Soot number density isosurface $N_s = 10^7$ m^{-3} colored by mean crystal radius r_p (m) for $N_b = 0.012$ s^{-1}. Comparison between RANS initialization strategy and 4LO initialization strategy. Distances are in meters.

450 pair. For the two cases, we observe the development of short-wave instabilities on the vortex tubes that are responsible for the

https://doi.org/10.5194/egusphere-2025-1865
Preprint. Discussion started: 26 May 2025

wavy aspect of the vortex tubes. These instabilities are typical of quadripolar vortex systems in a counter-rotating configuration theoretically (see Fabre et al. (2002) theoretical study) and were not observed for the 2LO initialization as it can be seen in Fig.21 of Bouhafid et al. (2024). However, Widnall instability for vortex pairs, theorized in Tsai and Widnall (1976), may also occur as observed in Holzäpfel et al. (2001), despite not being observed in a comparable case studied by Picot et al. (2014). The absence of Widnall instability on the vortex pair for the 2LO initialization can be explained as follows.

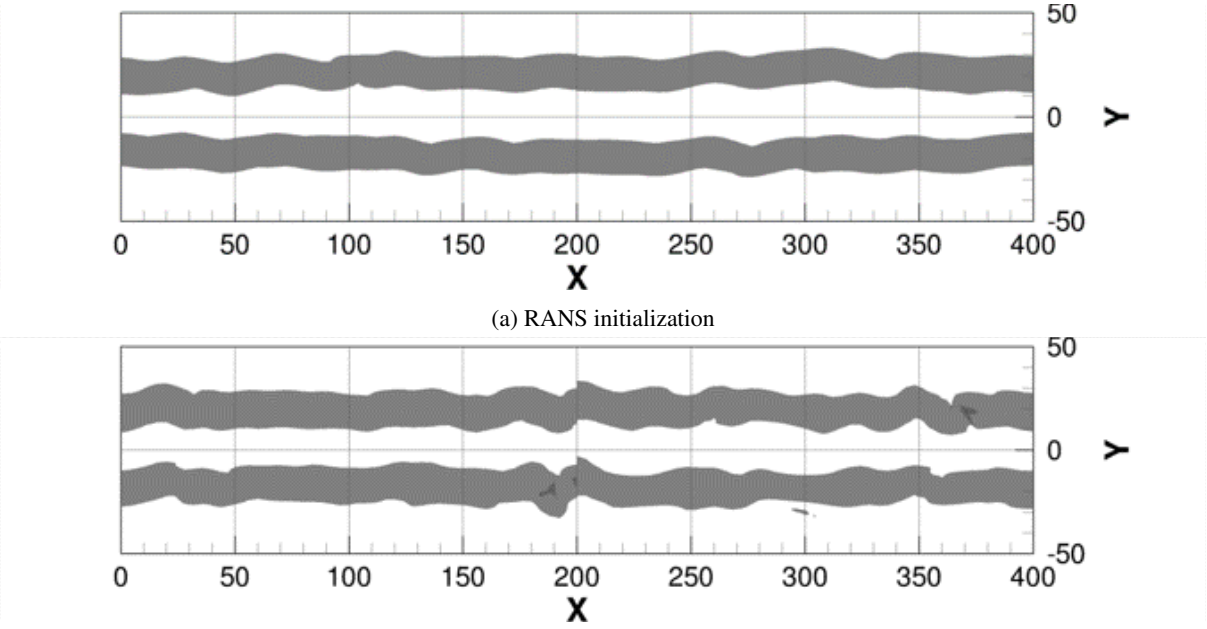

(a) RANS initialization

(b) 4LO initialization

Figure 13. 2D view of Q-criterion isosurface $Q = 0.03\ \mathrm{s}^{-1}$ at $t/t_b = 3.89$ for RANS initialization and 4LO initialization. Distance are in meters.

Widnall instability occurs in vortex pairs and is due to a resonance phenomenon between the transverse shear caused by one vortex on the other, and the existence of Kelvin waves with the same wavenumber k and azimuthal wavenumbers m and $m+2$. For a pair of Lamb–Oseen vortices, Sipp and Jacquin demonstrated in Sipp and Jacquin (2003) that a narrow band of Widnall instabilities exists only for Kelvin waves with $m = \pm 1$. The width of this instability band thus depends on the wavenumber k_w of the Kelvin modes, the ratio r_c/b_0 between the vortex core radius and the distance between the vortices, and two real constants. The instability bands for the first three modes are given by:

$$2.26 - 8.68 r_c^2/b_0^2 < k r_c < 2.26 + 8.68 r_c^2/b_0^2 \tag{20}$$

$$3.96 - 14.4 r_c^2/b_0^2 < k r_c < 3.96 + 14.4 r_c^2/b_0^2 \tag{21}$$

https://doi.org/10.5194/egusphere-2025-1865
Preprint. Discussion started: 26 May 2025

$$5.61 - 20.1 r_c^2/b_0^2 < k r_c < 5.61 + 20.1 r_c^2/b_0^2 \tag{22}$$

The numerical application for the case considered in this work gives $r_c^2/b_0^2 = 5.75 \times 10^{-3}$ at $t = 0$, leading to very narrow instability bands. Consequently, the absence of Widnall instabilities in the LES using a dipolar analytical initialization from two Lamb–Oseen vortices could be explained by the fact that the perturbation wavenumber lies outside these instability bands.

The temporal LES simulation performed by Holzäpfel et al. (2001) using a dipolar analytical initialization strategy displayed the Widnall instability on the vortex pair. The appearance of these instabilities can be explained by the synthetic turbulence approach used to model wake turbulence and atmospheric turbulence. First, wake turbulence was added directly in the vortices while atmospheric turbulence was added in the whole domain. Second, the corresponding synthetic wake turbulence fluctuations generated in the simulation by Holzäpfel et al. (2001) were distributed according to a normal distribution and are, therefore, not spatially correlated. As a result, their perturbation energy does not depend on their size and short-wave Widnall instability modes can potentially be excited with sufficient energy.

By contrast, the temporal LES simulation by Picot in Picot et al. (2014) also used a pair of Lamb–Oseen vortices to initialize the vortex regime but did not introduce synthetic wake turbulence inside the vortices. In addition, atmospheric turbulence was generated through an Ornstein-Uhlenbeck forcing technique, which resulted in correlated turbulence following a realistic turbulence spectrum in a stratified fluid. No short-wavelength instability was then observed on the vortices.

Not adding synthetic turbulence in the vortices for a far-field flow calculation can be justified by two main reasons. First, the jet plume concentrates the vast majority of the turbulent kinetic energy. This is actually a consequence of the second point, which is that turbulence generated in a Lamb–Oseen vortex is rapidly destroyed in the jet regime because of rotation effects that were theoretically studied in Jacquin and Pantano (2002). Finally, in this work computations, the atmospheric turbulence is much closer to the one in Picot et al. (2014) work than the one from Holzäpfel et al. (2001) in terms of turbulent kinetic energy spectra and spatial correlations. This too may justify the absence of Windall instability in the 2LO case. Thus, it is believed that it is not the Windall instability that is observed in the RANS and 4LO cases, but the shortwave instabilities resulting from the four-vortex nature of the wake (see Fabre et al. (2002).

Fig.14 plots the relevant contrail dimensions as a function of time for the three different initialization strategies: RANS initialization, 2LO initialization and 4LO initialization. In terms of height and width, 4LO initialization gives a very similar contrail in terms of size compared to the RANS initialization. The contrail has a larger cross-section area for the 4LO initialization but is still much closer to the RANS initialization cross-section area than the 2LO initialization.

The evolution of averaged microphysical quantities is plotted in Fig.15. Despite the initial differences, the soot number density is almost identical at the end of the dissipation regime between the RANS and 4LO initialization. This emphasizes the additional mixing of the plume with ambient air caused by the turbulent nature of the wake. In terms of mean ice crystal radius and IWC, 4LO initialization gives slightly higher values than RANS initialization at the end of the simulation. However,

https://doi.org/10.5194/egusphere-2025-1865
Preprint. Discussion started: 26 May 2025

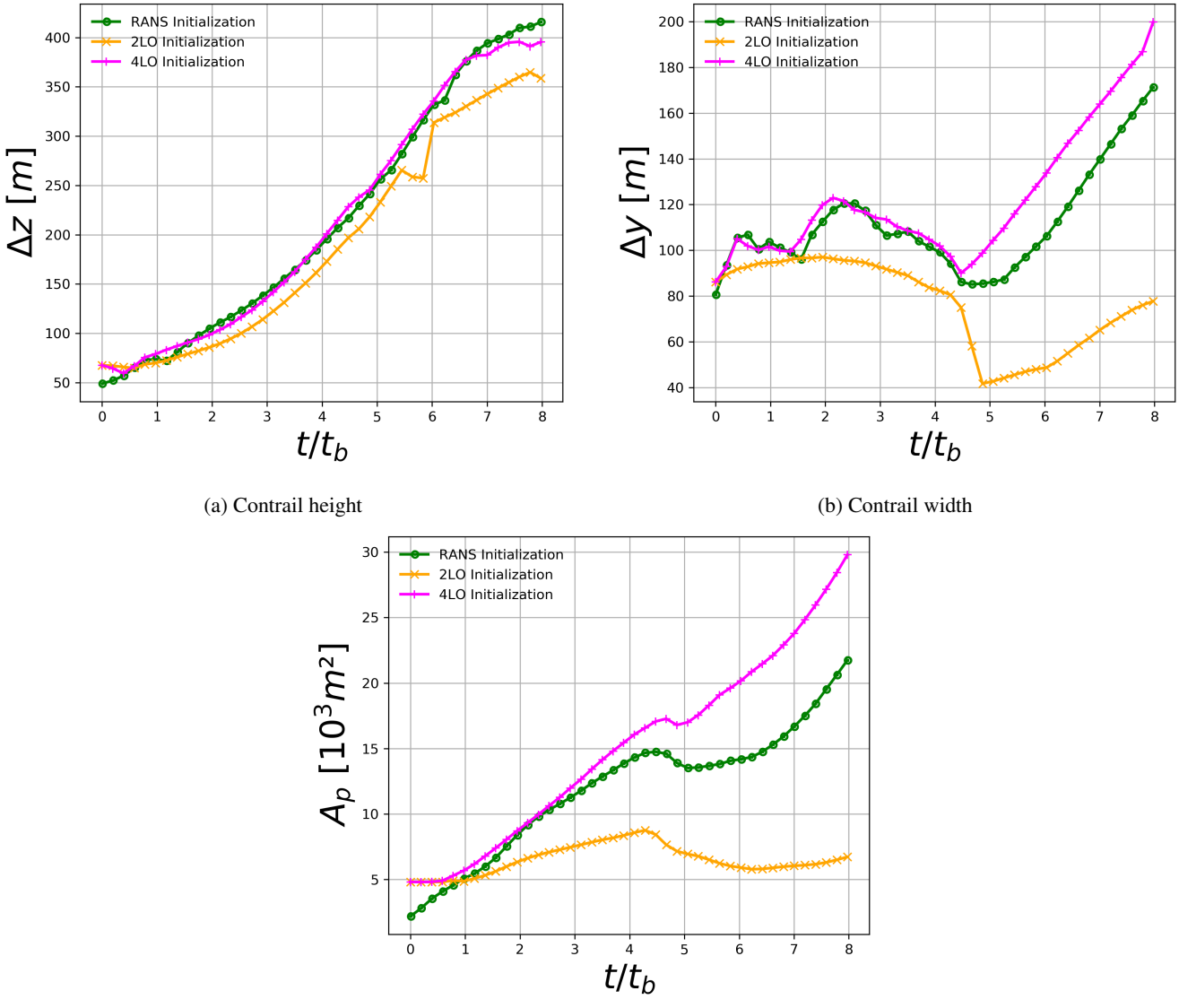

(a) Contrail height

(b) Contrail width

(c) Area of contrail cross-section

Figure 14. Contrail length scales for the different initialization strategies at $N_b = 0.012\ \mathrm{s}^{-1}$ (medium stratification scenario)

we observe that for the complete simulation, 4LO initialization results are qualitatively more similar to RANS initialization compared to 2LO initialization.

Fig.16 displays the evolution of the spatially averaged extinction E with time. The largest extinction is obtained for the 4LO initialization since the corresponding contrail was predicted to be wider with larger ice crystals on average. Contrary to 2LO initialization, the radiative forcing of young contrails will be overestimated. In light of that result, it appears that accurately estimating the radiative forcing of young contrails strongly depends on how the early aerodynamic of the near-field influences

https://doi.org/10.5194/egusphere-2025-1865
Preprint. Discussion started: 26 May 2025

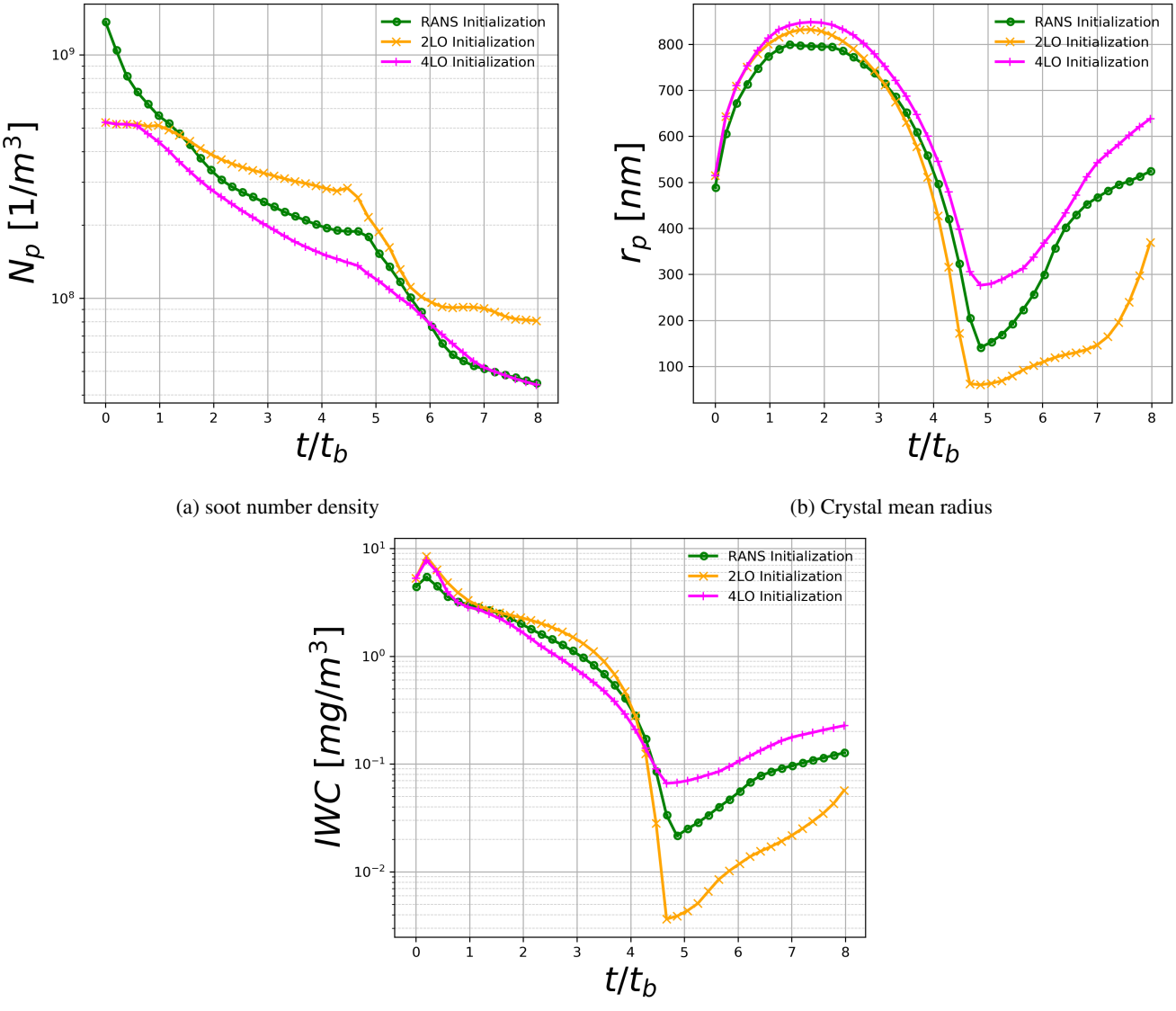

(a) soot number density

(b) Crystal mean radius

(c) Ice water content

Figure 15. Average contrail microphysics quantities for the different LES initialization strategies at $N_b = 0.012\ \mathrm{s}^{-1}$

the contrail in the far-field. Horizontal tailplane vortices, which are commonly neglected in most temporal LES of contrails and aircraft wakes, seem to play an important role. The differences observed between the RANS initialization and 4LO initialization could possibly be explained by the difference in strength for the shortwave instabilities. Indeed, it appears that the vortex tube deformation amplitude is higher for the 4LO initialization as seen in Fig.13. This might result in a more turbulent secondary wake and a wider contrail.

https://doi.org/10.5194/egusphere-2025-1865
Preprint. Discussion started: 26 May 2025

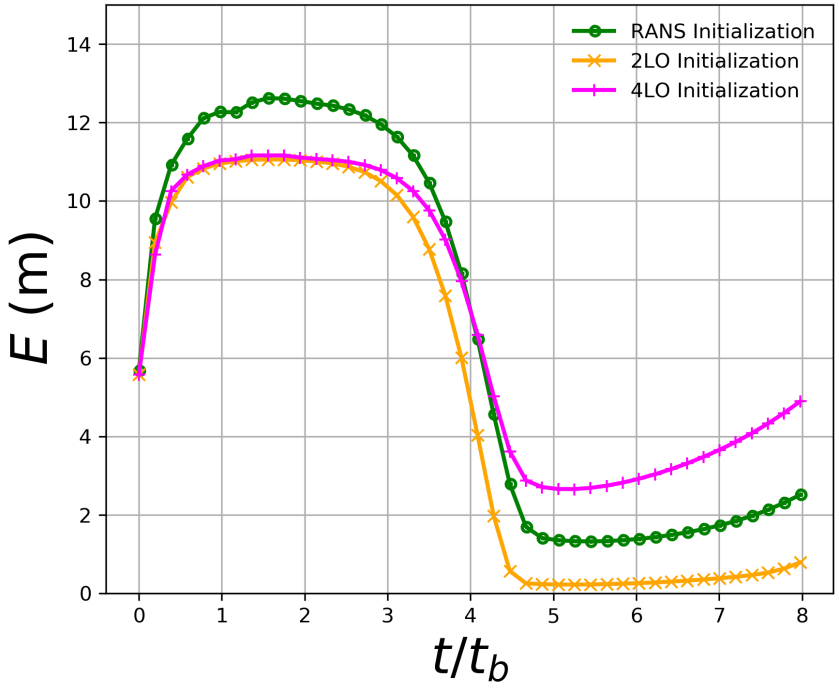

Figure 16. Average extinction as a function of time t. Comparison between the different initialization strategies for $N_b = 0.012\ \mathrm{s}^{-1}$.

5 Conclusions

This work extended the methodology of Bouhafid et al. (2024) to simulate young contrails for a realistic aircraft—from the formation of initial ice crystals to several minutes thereafter—without relying on analytical initialization. Instead, we directly solved the near-field aerodynamic wake and contrail formation using a RANS approach with a Reynolds-Stress turbulence model and then transitioned to far-field evolution with a temporal LES augmented by synthetic turbulence.

Applied to the B777-like CRM geometry under two stratification scenarios, our method revealed significant differences compared to classical analytical initialization using Lamb-Oseen vortices. In particular, RANS initialization produced a more turbulent contrail with greater size, larger ice crystals, and increased radiative impact. This behavior is attributed to short-wave instabilities inherent to a quadripolar vortex system in a counter-rotating configuration. A subsequent LES using four Lamb-Oseen vortices (representing two main wing-tip vortices and two HTP vortices) yielded contrail characteristics qualitatively similar to those from the RANS initialization.

These results are valid for young contrails under moderately ice-supersaturated conditions. Future work should assess whether these differences persist during the diffusion regime using Paoli et al. (2017) methodology and incorporate advanced microphysical models that account for soot activation, ice particle inertia, and background aerosol effects. Additionally, further investigation into the characteristics of HTP vortices and the impact of engine positioning (see Ramsay et al. (2024); Saulgeot

https://doi.org/10.5194/egusphere-2025-1865
Preprint. Discussion started: 26 May 2025

et al. (2023)) on contrail development could inform more effective contrail mitigation strategies through optimized aircraft design.

Author contributions. **Younes Bouhafid**: Writing – review & editing, Writing – original draft, Visualization, Validation, Methodology, Investigation, Formal analysis, Data curation, Conceptualization. **Nicolas Bonne**: Writing – review & editing, Validation, Methodology, Supervision, Formal analysis, Conceptualization.

Competing interests. The authors declare that they have no known competing financial interests or personal relationships that could have appeared to influence the work reported in this paper.

Acknowledgements. This research has been supported by the French Ministère de la Transition Ecologique et Solidaire under the CLIMAVIATION programme (grant No. DGAC N2021-39), with support from France's Plan National de Relance et de Résilience (PNRR) and the European Union's NextGenerationEU.

https://doi.org/10.5194/egusphere-2025-1865
Preprint. Discussion started: 26 May 2025

References

Birner, T.: Fine-scale structure of the extratropical tropopause region, Journal of Geophysical Research: Atmospheres, 111, https://doi.org/10.1029/2005JD006301, 2006.

Bouhafid, Y., Bonne, N., and Jacquin, L.: Combined Reynolds-averaged Navier-Stokes/Large-Eddy Simulations for an aircraft wake until dissipation regime, Aerospace Science and Technology, 154, 109 512, 2024.

Castro, H. G. and Paz, R. R.: A time and space correlated turbulence synthesis method for large eddy simulations, Journal of Computational Physics, 235, 742–763, https://doi.org/10.1016/j.jcp.2012.10.035, 2013.

Cho, J. Y. and Lindborg, E.: Horizontal velocity structure functions in the upper troposphere and lower stratosphere: 1. Observations, Journal of Geophysical Research: Atmospheres, 106, 10 223–10 232, https://doi.org/10.1029/2000JD900814, 2001.

Churchfield, M. J. and Blaisdell, G. A.: Numerical simulations of a wingtip vortex in the near field, Journal of Aircraft, 46, 230–243, https://doi.org/10.2514/1.38086, 2009.

Crow, S. and Bate Jr, E.: Lifespan of trailing vortices in a turbulent atmosphere, Journal of Aircraft, 13, 476–482, https://doi.org/10.2514/3.44537, 1976.

Crow, S. C.: Stability theory for a pair of trailing vortices, AIAA journal, 8, 2172–2179, https://doi.org/10.2514/3.6083, 1970.

Fabre, D., Jacquin, L., and Loof, A.: Optimal perturbations in a four-vortex aircraft wake in counter-rotating configuration, Journal of Fluid Mechanics, 451, 319–328, https://doi.org/10.2514/6.2023-3889, 2002.

Ferreira, T., Caprace, D., Paoli, R., Shariff, K., and Lele, S.: Can inducing the Crow instability reduce contrail radiative forcing?, in: Proceedings of the Summer Program, p. 1, 2024.

Garnier, F., Baudoin, C., Woods, P., and Louisnard, N.: Engine emission alteration in the near field of an aircraft, Atmospheric Environment, 31, 1767–1781, 1997.

Gerz, T., Dürbeck, T., and Konopka, P.: Transport and effective diffusion of aircraft emissions, Journal of Geophysical Research: Atmospheres, 103, 25 905–25 913, https://doi.org/10.1029/98JD02282, 1998.

Grise, K. M., Thompson, D. W., and Birner, T.: A global survey of static stability in the stratosphere and upper troposphere, Journal of Climate, 23, 2275–2292, https://doi.org/10.1029/2007JD009022, 2010.

Holzäpfel, F., Gerz, T., and Baumann, R.: The turbulent decay of trailing vortex pairs in stably stratified environments, Aerospace Science and Technology, 5, 95–108, https://doi.org/10.1016/S1270-9638(00)01090-7, 2001.

Hulst, H. C. and van de Hulst, H. C.: Light scattering by small particles, Courier Corporation, 1981.

Jacquin, L. and Garnier, F.: On the dynamics of engine jets behind a transport aircraft, Report No. AGARD CP-584 (NATO, Brussels), 1996.

Jacquin, L. and Pantano, C.: On the persistence of trailing vortices, Journal of Fluid Mechanics, 471, 159–168, https://doi.org/10.1017/S0022112002002161, 2002.

Kärcher, B.: Physicochemistry of Aircraft Generated Liquid Aerosols, Soot, and Ice Particles: Model Description, J. Geophys. Res., https://doi.org/10.1029/98JD01044, 1998.

Khou, J.-C.: Modélisation des traînées de condensation par interaction entre l'aérodynamique, la cinétique chimique et la microphysique, Ph.D. thesis, Université Pierre et Marie Curie-Paris VI, 2016.

Khou, J.-C., Ghedhaifi, W., Vancassel, X., and Garnier, F.: Spatial simulation of contrail formation in near-field of commercial aircraft, Journal of Aircraft, 52, 1927–1938, https://doi.org/10.2514/1.C033101, 2015.

https://doi.org/10.5194/egusphere-2025-1865
Preprint. Discussion started: 26 May 2025

Lee, D. S., Fahey, D. W., Skowron, A., Allen, M. R., Burkhardt, U., Chen, Q., Doherty, S. J., Freeman, S., Forster, P. M., Fuglestvedt, J., et al.: The contribution of global aviation to anthropogenic climate forcing for 2000 to 2018, Atmospheric Environment, 244, 117 834, https://doi.org/10.1016/j.atmosenv.2020.117834, 2021.

Lewellen, D. and Lewellen, W.: The effects of aircraft wake dynamics on contrail development, Journal of the atmospheric sciences, 58, 390–406, https://doi.org/10.1175/1520-0469(2001)058<0390:TEOAWD>2.0.CO;2, 2001.

Loseille, A. and Alauzet, F.: Continuous mesh framework part I: well-posed continuous interpolation error, SIAM Journal on Numerical Analysis, 49, 38–60, https://doi.org/10.1137/090754078, 2011a.

Loseille, A. and Alauzet, F.: Continuous mesh framework part II: validations and applications, SIAM Journal on Numerical Analysis, 49, 61–86, https://doi.org/10.1137/10078654X, 2011b.

Misaka, T., Holzäpfel, F., and Gerz, T.: Large-eddy simulation of aircraft wake evolution from roll-up until vortex decay, AIAA journal, 53, 2646–2670, https://doi.org/10.2514/1.J053671, 2015.

Montreuil, E., Ghedhaifi, W., Chmielaski, V., Vuillot, F., Gand, F., and Loseille, A.: Numerical Simulation of contrail formation on the Common Research Model wing/body/engine configuration, in: 2018 Atmospheric and Space Environments Conference, p. 3189, https://doi.org/10.2514/6.2018-3189, 2018.

Murphy, D. M. and Koop, T.: Review of the vapour pressures of ice and supercooled water for atmospheric applications, Quarterly Journal of the Royal Meteorological Society: A journal of the atmospheric sciences, applied meteorology and physical oceanography, 131, 1539–1565, 2005.

Paoli, R., Nybelen, L., Picot, J., and Cariolle, D.: Effects of jet/vortex interaction on contrail formation in supersaturated conditions, Physics of Fluids, 25, https://doi.org/10.1063/1.4807063, 2013.

Paoli, R., Thouron, O., Cariolle, D., García, M., and Escobar, J.: Three-dimensional large-eddy simulations of the early phase of contrail-to-cirrus transition: effects of atmospheric turbulence and radiative transfer, Meteorologische Zeitschrift (Berlin), 26, https://doi.org/10.1127/metz/2017/0764, 2017.

Petzold, A. and Schröder, F. P.: Jet engine exhaust aerosol characterization, Aerosol Science and Technology, 28, 62–76, https://doi.org/10.1080/02786829808965512, 1998.

Petzold, A., Döpelheuer, A., Brock, C., and Schröder, F.: In situ observations and model calculations of black carbon emission by aircraft at cruise altitude, Journal of Geophysical Research: Atmospheres, 104, 22 171–22 181, https://doi.org/10.1029/1999JD900460, 1999.

Picot, J., Paoli, R., Thouron, O., and Cariolle, D.: Large-eddy simulations of contrails in a turbulent atmosphere, Atmospheric Chemistry & Physics Discussions, 14, 29 499–29 546, https://doi.org/doi:10.5194/acpd-14-29499-2014, 2014.

Pope, S. B.: Turbulent flows, Measurement Science and Technology, 12, 2020–2021, https://doi.org/10.1088/0957-0233/12/11/705, 2001.

Ramsay, J., Tristanto, I., Shahpar, S., and John, A.: Assessing the Environmental Impact of Aircraft/Engine Integration With Respect to Contrails, Journal of Engineering for Gas Turbines and Power, 146, https://doi.org/10.1115/1.4066150, 2024.

Refloch, A., Courbet, B., Murrone, A., Villedieu, P., Laurent, C., Gilbank, P., Troyes, J., Tessé, L., Chaineray, G., Dargaud, J., et al.: CEDRE software, Aerospace Lab, pp. p–1, 2011.

Saulgeot, P., Brion, V., Bonne, N., Dormy, E., and Jacquin, L.: Effects of atmospheric stratification and jet position on the properties of early aircraft contrails, Physical Review Fluids, https://doi.org/https://doi.org/10.1103/PhysRevFluids.8.114702, 2023.

Schumann, U., Baumann, R., Baumgardner, D., Bedka, S. T., Duda, D. P., Freudenthaler, V., Gayet, J.-F., Heymsfield, A. J., Minnis, P., Quante, M., et al.: Properties of individual contrails: a compilation of observations and some comparisons, Atmospheric Chemistry and Physics, 17, 403–438, https://doi.org/10.5194/acp-17-403-2017, 2017.

https://doi.org/10.5194/egusphere-2025-1865
Preprint. Discussion started: 26 May 2025

Schwamborn, D. and Strelets, M.: ATAAC–An EU-project dedicated to hybrid RANS/LES methods, in: Progress in Hybrid RANS-LES Modelling: Papers Contributed to the 4th Symposium on Hybrid RANS-LES Methods, Beijing, China, September 2011, pp. 59–75, Springer, https://doi.org/10.1007/978-3-642-31818-4_5, 2012.

Sipp, D. and Jacquin, L.: Widnall instabilities in vortex pairs, Physics of Fluids, 15, 1861–1874, 2003.

Tabazadeh, A., Martin, S. T., and Lin, J.-S.: The effect of particle size and nitric acid uptake on the homogeneous freezing of aqueous sulfuric acid particles, Geophysical research letters, 27, 1111–1114, https://doi.org/10.1029/1999GL010966, 2000.

Tsai, C.-Y. and Widnall, S. E.: The stability of short waves on a straight vortex filament in a weak externally imposed strain field, Journal of Fluid Mechanics, 73, 721–733, https://doi.org/doi.org/10.1017/S0022112076001584, 1976.

Unterstrasser, S.: Large-eddy simulation study of contrail microphysics and geometry during the vortex phase and consequences on contrail-to-cirrus transition, Journal of Geophysical Research: Atmospheres, 119, 7537–7555, https://doi.org/10.1002/2013JD021418, 2014.

Unterstrasser, S. and Görsch, N.: Aircraft-type dependency of contrail evolution, Journal of Geophysical Research: Atmospheres, 119, 14–015, https://doi.org/10.1002/2014JD022642, 2014.

Voigt, C., Kleine, J., Sauer, D., Moore, R. H., Bräuer, T., Le Clercq, P., Kaufmann, S., Scheibe, M., Jurkat-Witschas, T., Aigner, M., et al.: Cleaner burning aviation fuels can reduce contrail cloudiness, Communications Earth & Environment, 2, 114, 2021.

Wilcox, D. C. et al.: Turbulence modeling for CFD, vol. 2, DCW industries La Canada, CA, 1998.